REVIEW

Solid-state polymer electrolytes in lithium batteries: latest progress and perspective

Jingbo Mu,[a] Shimin Liao,[a] Linlin Shi,[b] Bihai Su,[b] Feng Xu,[b] Zengcai Guo, [ID] *[a] Hailing Li[a] and Fangfang Wei*[a]

The increasing demands for battery performance in the new era of energy necessitate urgent research and development of an energy storage battery that offers high stability and a long service life. Among the various types of batteries available, the all-solid lithium battery emerges as the preferred choice because of its exceptional safety, stability, and sustainability features. The solid electrolyte plays a crucial role in facilitating efficient energy transmission within the structure of the lithium battery. Solid electrolytes based on polymer chemistry can be classified into different categories, such as ether-based, ester-based, nitrile-based, and polyvinylidene fluoride materials. This discussion also covers topics such as ion transport mechanisms, levels of ionic conductivity, techniques for modification, and analysis of cyclic stability specifically for lithium-ion batteries utilizing solid electrolytes. Finally, an outlook on the future research direction of solid-state polymer electrolytes is suggested for commercially large-scale production and application.

1. Introduction

In recent times, significant advances have been made in the conversion and storage of energy batteries. Solid-state electrolytes (SSEs) have emerged as crucial components in the utilization of new-energy trams and everyday electronic devices due to their exceptional energy density, consistent power output, and extended lifespan. Compared to nickel metal hydride batteries, they find superior application prospects within the electric vehicle domain. As research progresses, there is an urgent need to enhance the energy density of rechargeable lithium-ion batteries. The utilization of lithium as an anode brings it closer to attaining its highest theoretical specific energy density (3862 mA h g^{-1}).[1–7] Researchers have devised various approaches to improve the performance of lithium ion batteries, such as incorporating modified electrolyte additives,[8–12] implementing protective layers for the diaphragm,[13,14] and using superior matrix materials.[15–17] Some lithium batteries employ organic liquid electrolytes, which are prone to volatilization, leakage, and drying while exhibiting unstable chemical properties that increase the risk of explosions.[18–20] Consequently, to ensure the safe utilization of lithium ions, we proposed a gel polymer electrolyte in which a small quantity of

liquid organic solvent is added as a plasticizer and immobilized within the gel polymer. The most efficient technique involves substituting solid electrolytes for organic liquid. This method not only improves the energy efficiency of the battery, but also addresses issues related to short life expectancy and instability.[21–23] Furthermore, due to their high thermal stability and low flammability characteristics along with their ability to prevent leakage or volatilization incidents, thus eliminating risks associated with fire or explosions; solid-state electrolytes facilitate the development of secure and stable solid-state batteries.[24–28]

The conductivity of solid electrolytes has gradually approached or even exceeded that of a liquid electrolyte. However, the effective transport of lithium ions in batteries is hindered by interface impedance, which arises from element diffusion and interface reactions between the solid electrolyte and the cathode material. To address this problem, common approaches involve applying coatings to the cathode material and modifying the surface of the electrolyte.[29,30]

In addition, the presence of lithium dendrites is a common issue in lithium-ion batteries. However, the utilization of solid electrolytes can effectively mitigate the risk of short circuits between electrodes, making it more suitable for applications in microelectronics or portable equipment. Integrating the diaphragm with the electrolyte in solid electrolyte technology enhances ionic conductivity.[31–33] The selection of electrolyte materials plays a crucial role in determining the operational mechanism of batteries, impacting factors such as specific energy, safety, cycle performance, rate charge–discharge performance, energy storage capabilities, and the cost of lithium

[a] Key laboratory of new energy development and energy storage technology of Handan, College of Materials Science and Engineering, Hebei University of Engineering, Handan 056038, People's Republic of China.
E-mail: guozengcai@sina.com, fangfangwei@hebeu.edu.cn
[b] Hebei Gellec New Energy Science&Technology Co., Ltd, Handan 057150, People's Republic of China

batteries.[34,35] As a result, future research can focused on the following directions: (1) design of single lithium-ion polymer electrolytes, in which the anions are immobilized by trapping agents or functional groups of polymers.[36,37] (2) Decreasing the electrolyte/electrode interfacial resistance and interface impedance in the cathode.[38] (3) Improving the lithium ion conductivity of SPEs at room temperature or even low temperature.[39,40] (4) Prepare polymer electrolyte with special structure by template method and self-assembly method to optimize the lithium ion diffusion path.[41,42] (5) In conjunction with *in situ* characterization of the lithium dendrite growth process, optimizing the interface composition and reducing the occurrence of side reactions.[43,44]

The modification of SSEs made from polymers has achieved remarkable success thus far. This paper initially explores the mechanism behind the growth of lithium dendrites in these electrolytes. Subsequently, it provides a comprehensive overview of various design approaches for SSEs with various chemical structures such as ether, ester, nitrile, and vinylidene fluoride (Fig. 1b). Generally, the use of different types of polymers

is related to the stable use of batteries (Fig. 1c). The aim of this research is not only to offer guidance in developing polymer materials for solid electrolytes but also to assist in optimizing the interface reaction within all-solid-state lithium batteries. Ultimately, this optimization will lead to enhanced electrochemical performance and enable practical applications.

2. Interfacial diffusion of lithium ions

The solid electrolyte interface, commonly referred to as the SEI, facilitates the movement of lithium ions within its solid phase. The ion migration mechanism is intricately linked to the structural characteristics of the crystals.[45–48] The conductivity is greatly influenced by the different transport mechanisms of lithium ions in different systems. Therefore, understanding the transportation process of lithium ions in solid electrolytes plays a crucial role in designing materials with enhanced performance.[51]
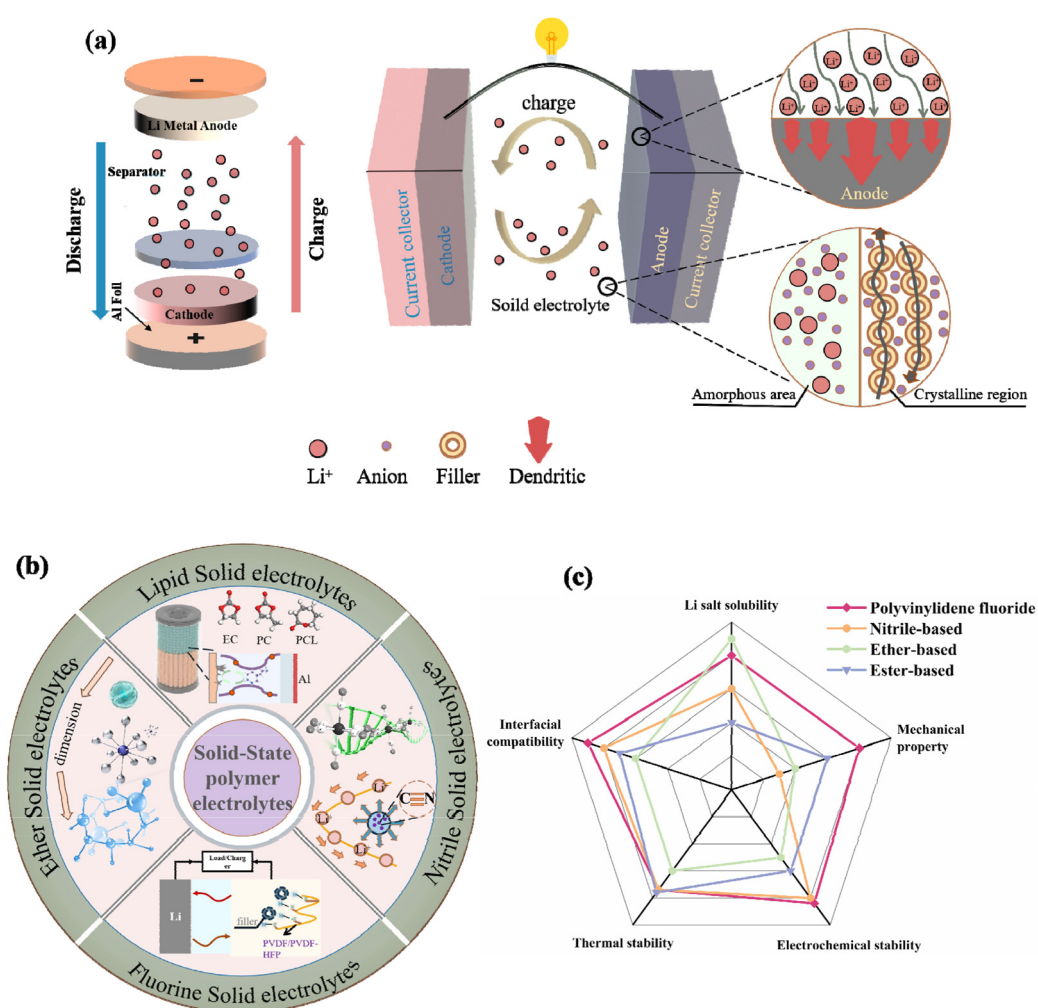

Fig. 1 Schematic illustration of a battery. (a) Li$^+$ transport in polymer electrolytes and growth of lithium dendrites, (b) typical polymer electrolytes, (c) Radar map of properties of different polymers.

Time correlation functions for the transportation of Li$^+$ ions. The van Hove time correlation function characterizes the likelihood of locating a displaced Li$^+$ ion at time t, with a displacement of r from its initial position. This van Hove function can be divided into two components, namely self and distinct parts, denoted as $G(r, t) = G_s(r, t) + G_d(r, t)$, where the latter exhibits the following forms.

$$G(r,t) = \frac{1}{N} \left\langle \sum_{i=1}^{N} \sum_{j=1}^{N} \delta(r + r_j(0) - r_i(t)) \right\rangle \quad (1)$$

$$G_d(r,t) = \frac{1}{N} \left\langle \sum_{j=1}^{N} \delta(r + r_j(0) - r_i(t)) \right\rangle \quad (2)$$

At time $t = 0$, the van Hove function simplifies the pair correlation function in a stationary state.

$$G(r,0) = \delta(r) + pg(r) \quad (3)$$

The jump probability is determined by the self-component of the van Hove function, and it is commonly approximated using a Gaussian model as an initial estimation.

$$G_s(r,t) = \left[\frac{3}{2\pi\langle\Delta r(t)^2\rangle} \right]^{3/2} \exp\left[-\left(\frac{3r^2}{2\langle\Delta r(t)^2\rangle} \right) \right] \quad (4)$$

For fluids such as EC, the reliability of this Gaussian behavior can be expected. On the other hand, in the trapping regime of EDC, $G_s(r,t)$ demonstrates a depletion of probability near the limits of the traps (Fig. 2, adapted from ref. 49), $r > \langle\Delta r(t)^2\rangle^{1/2}$ with a subsequent redistribution of that probability at shorter and longer distances. The departure from Gaussian behavior can be quantified by assessing the non-Gaussian parameter.[50]

$$\alpha(t) = \frac{3\langle\Delta r(t)^4\rangle}{5\langle\Delta r(t)^2\rangle^2} - 1 \quad (5)$$

2.1 Interfacial evolution of Li dendrites

Polymer electrolyte is a unique type of SSEs. Polymer electrolytes have limited mechanical strength, making them susceptible to penetration by lithium filaments (see Fig. 1a). The transportation of ions occurs through coordinated Li ions along the polymer chains. The propagation of dendrite in polymer SSEs resembles that in liquid electrolytes. Monroe *et al.* conducted simulations to study the dendrite formation process in polymer SSE.[52] In summary, interfacial kinetics are primarily influenced by surface homogeneity and current density. The introduction of a lithium alloy helps reduce the overpotential for Li deposition and inhibits the penetration of Li dendrites. Even on rough surfaces, high current density is used to guide the deposition of Li to achieve high rate stability of the battery.

2.1.1 Hard short circuit. The occurrence of hard short circuits in solid-state lithium–metal batteries (SSLMBs) is the result of the rapid infiltration of dendrites that establish direct connections between the anode and cathode, rendering recovery impossible. These dendrites can be considered as parallel leakage resistance within the impedance spectra fitting circuit. During galvanostatic measurements, a sudden and significant decrease in voltage or polarization levels is observed.[53] Predicting such hard short circuits is challenging.[54,55] In certain scenarios, these hard shorts coincide with pronounced polarizations. Typically found within rigid inorganic SSEs. In particular, regions with lower strength, such as grain boundaries and defects, demonstrate a reduced shear modulus compared to those of bulk solid-state electrolytes. These areas are particularly favorable for the complete propagation of dendrites.[55]

2.1.2 Partly short circuit. The initial stage of a complete short circuit is characterized by a partial short circuit, which may pause or terminate subsequently. During this process, the lithium filaments penetrate only the interfaces rather than the entire bulk SSEs. As a result, there is a slight drop in polariz-
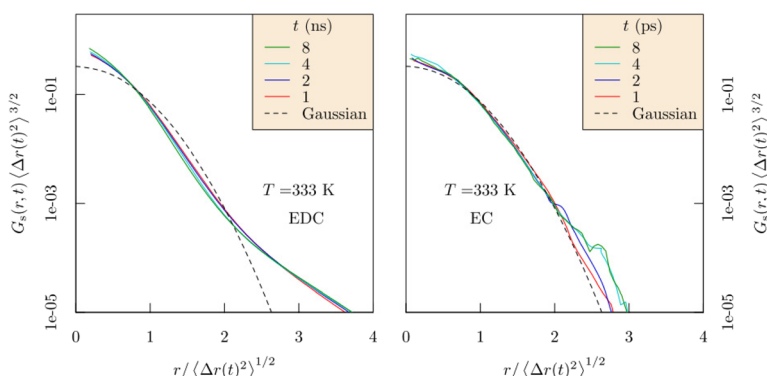
Fig. 2 Dimensionally scaled $G_s(r,t)$ for Li$^+$ ions as it depends on displacement for increasing times in EDC (left) and EC (right). Though the Gaussian model (dashed curve) is reliable in EC solvent, the probability is depleted near the trap boundaries, $r > \langle\Delta r(t)^2\rangle^{1/2}$, and replaced at shorter and longer distances for EDC. Note that these correlations decay in a few ps for EC, but require ns for EDC ref. 49. Copyright 2017, The Electrochemical Society.

ation voltage, indicating a partial reduction in the bulk impedance.[56] It should be noted that because of the presence of bulk electrolyte impedance, a partially short circuit cannot be considered as a complete failure of a solid-state battery. According to Lu *et al.*, an increase in external currents will lead to an increase in polarization following Ohm's law.[57,58]

2.1.3 Soft short circuit. The soft short circuit refers to a minor decrease in voltage during battery operation, which is evident in the significant fluctuations observed in charging curves. Adjusting external factors such as current density, pressure, or temperature, it is possible to recover from this soft short circuit phenomenon.[59] This type of short circuit typically occurs in polymer electrolytes or solid–liquid hybrid electrolytes. Unlike rigid inorganic materials, polymers possess some degree of fluidity that allows for uniform interfacial contact. The soft short circuit arises from the formation and dissolution of small dendrites. However, due to the high viscosity of the polymer/partial liquid systems, these dendrites remain small and can easily merge again, offering opportunities for battery recovery.[59] However, it should be noted that soft short circuits may lead to excessive charging behavior, resulting in waste of energy.

2.1.4 Design for low electronic conductivity. Regardless of the type of solid polymer and processing conditions, the problem of lithium dendrites will persist, the inhomogeneity of the interface stands out as one of the most prevalent factors, which originates from the microstructural defect at the physical interface between lithium metal and solid polymer, resulting in localized high current density due to resistance shrinkage. Hence, the favorable development of lithium metal is induced by the presence of high local current density. To prevent excessive electronic conductivity within the system, Sunyoung Lee *et al.* have successfully addressed the issue of inadequate interface contact and electron leakage through their innovative design involving layer-by-layer components comprising a lithium-attracting layer (Ag) and an electron-blocking layer (LiF), as illustrated in Fig. 3(a and b). The existence of lithium philic layer contributes to the homogenization of lithium flux and keeps it well moist. The electron barrier layer fundamentally passivates the electron transport path at the interface, thereby preventing the nucleation of solid electrolyte lithium caused by electron leakage. The lithium symmetric electrode achieves a critical density (CCD) of 3.1 mA cm^{-2} at a temperature of 60 °C, as shown in Fig. 3c. The effectiveness of this approach is validated by the distinctive design of the interface layer.[60]

Based on this premise, Hantao Xu *et al.* aimed to enhance the mechanical strength and ion transport dynamics of solid-state electrolytes (SSEs). To achieve this, they employed a polymer design strategy and cross-linked poly1-3-dioxopentane to create a topological polymer known as CPDOL. This was then used to form an *in situ* topological polymer interface layer with lithium metal. As depicted in Fig. 3d, the structural system comprises a significant quantity of LiF components that effectively impede electron flow and suppress side reactions at the interface. As depicted in Fig. 3e, the CPLAR-SPE

LFP/Li battery exhibits a consistent and enduring cycling performance, achieving a capacity of 116.5 mA h g^{-1} after undergoing 500 cycles at a rate of 0.5 C. Moreover, it consistently maintains an average Coulomb efficiency exceeding 99.78%, further validating the establishment of a steadfast electron-blocking layer that effectively hinders the proliferation of lithium dendrites.[61]

To emphasize the significance of interface stability, Long Hu *et al.* utilized an interlayer design (as depicted in Fig. 3f) to create an ion/electron conductive layer with the aid of fillers. By incorporating conductive TiN particles into a PEO-based solid electrolyte, we successfully obtained a polymer electrolyte with mixed ion/electronic properties. Additionally, an insulating LiYF$_4$ filler was utilized. During the cycling process, the prepared PEO-TiN/PEO-LiYF$_4$/PEO-TiN film formed a LiN interface. Moreover, the presence of PEO-TiN effectively prevented lithium dendrite penetration into the intermediate layer of PEO-LiYF$_4$ by consuming it on its own. This remarkable electrochemical compatibility is demonstrated in Fig. 3g, where a capacity of 150 mA h g^{-1} was achieved after 50 cycles. These findings highlight the exceptional performance exhibited by soft pack batteries.[62]

3. Polyether-based solid polymer electrolytes

The presence of the chemical structure of –C–O–C in polyethers allows dissociation and complexation upon the addition of lithium salts, thus promoting relatively stable ion dynamics as a result of the flexible nature of the chain segments.[63–68] In the course of polyether-based solid polymer electrolytes (SPEs) development over the years, poly(ethylene oxide) (PEO) has emerged as the most widely used polymer electrolyte. Within this category, polyethylene glycol (PEG) shares a structure similar to PEO but has a lower molecular weight (<20 000). Despite its advantageous short-chain molecular structure that enhances molecular mobility, it does compromise the mechanical strength of SPEs. Consequently, PEG is frequently used as a preparatory precursor and modified inorganic filler to enhance its dispersion properties.[69,70]

PEO is the most widely used polymer electrolyte matrix material. PEO exhibits excellent coordination with lithium ions, thus influencing the transportation of cations through its complex chain segment.[71,72] At ambient temperature, the utilization of PEO polymer electrolyte results in the presence of three distinct phases: a crystalline phase (pure PEO phase), an amorphous phase (amorphous region) and a salt-rich phase. The conduction of lithium ions exclusively occurs within the amorphous region of the PEO polymer electrolyte, while exhibiting low ionic conductivity within the crystalline region.[73–76] Given that the room-temperature conductivity of PEO polymer is considerably low, enhancing its conductivity necessitates an increase in temperature to expand the amorphous region. However, since most lithium-ion batteries operate at room temperature, the substrate must be modified to improve
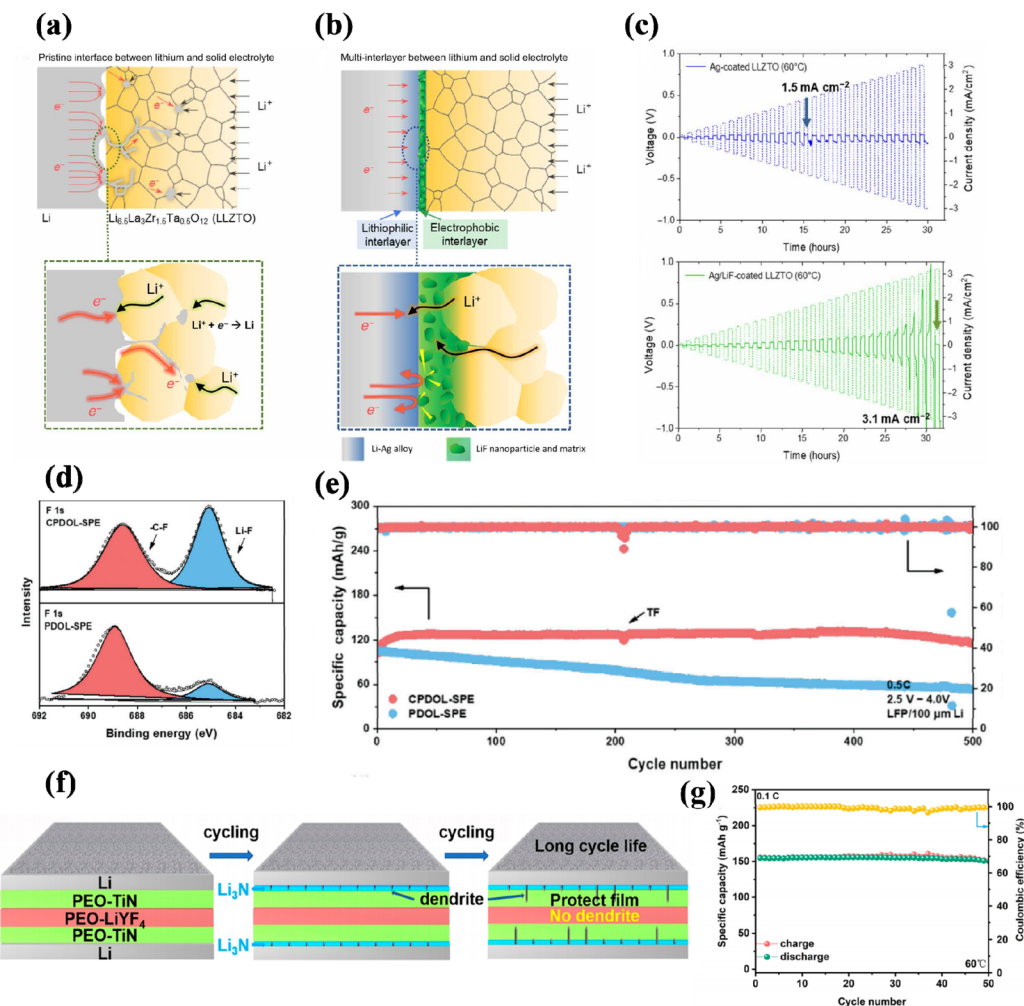
Fig. 3 (a) Lithium dendrite formation at the conventional interface between lithium metal and the sintered solid electrolyte. (b) Interfacial design coupling with lithiophilic and electron-blocking interlayers. CCD of (c) Ag-coated and Ag/LiF-coated LLZTO in lithium symmetric cells at 60 °C with increasing current densities ranging from 0.1 to 3.2 mA cm^{-2} at a step size of 0.1 mA cm^{-2} (ref. 60). Copyright 2023, Amer Assoc Advancement Science. (d) XPS spectra of F 1s of cycled CPDOL-based SEI and PDOL-based SEI. (e) Cycling performance of LiFePO$_4$/100 μm Li at 0.5 C (ref. 61). Copyright 2020, Wiley-VCH (f) schematic illustration of the cyclic evolution between sandwich-CPE and Li metal and the suppression of Li dendrite processes in a lithium symmetric cell. (g) Cycle performance of the pouch cell at 0.1 C under 60 °C (ref. 62). Copyright 2020, American Chemical Society.

performance.[77,78] PEO-based SPEs were first discovered by Wright *et al.* back in 1973.[79] Reinforcing the polymer matrix with nanoscale fillers and nanostructures facilitated the development of non-crystalline sections in PEO, as depicted in (Fig. 1a). The inclusion of such nanostructures resulted in the enlargement of disordered regions within the polymer, thereby enhancing the extent of amorphous areas and ultimately improving ionic conductivity.

3.1 Polyether-based solid electrolyte modified by nanofiller

Compared to conventional inorganic additives, nanomaterials possess a greater specific surface area. By incorporating these nanomaterials into the electrolyte, it is possible to enhance the cell capacity and shorten the pathway for lithium transport, thus facilitating its movement.[80–85] Nanofillers can be structured as ordered arrangements of nanoscale particles (0

dimensions), nanofibers (1 dimension), nanosheets (2 dimensions) or skeleton frame structures (3 dimensions) that are tailored for their mechanical and electrochemical properties. Research has indicated that the inclusion of inorganic nanofillers can mitigate the degradation of mechanical properties caused by low crystallinity in polyether-based solid polymer electrolytes. Moreover, these fillers have the potential to reduce interfacial impedance and enhance ionic conductivity, which are crucial factors in the design of high-performance electrolytes for energy storage systems.

3.1.1 Nanoparticles modifying SSEs. The addition of nanoparticles (such as LAGP and ZIF) is thought to hinder the local recombination of chains in the polymer, reduce polymer crystallization, and facilitate the high transport of lithium ions. At the same time, many studies have shown that the Lewis acid–base interaction model also supports an increase in the ionic

conductivity, which is an interesting area and avenue to improve the electrochemical performance of composite polymer electrolytes.

To prevent polymer crystallization and enhance the performance of solid-state electrolytes, Kondori *et al.* employed a physical approach by incorporating nanofillers into the electrolyte matrix to lower its glass transition temperature (T_g). They introduced $Li_{10}GeP_2S_{12}$ (LGPS) nanoparticles into a PEO-based electrolyte, followed by chemical bonding using mPEO, which significantly increases the proportion of amorphous regions without phase separation and improves ionic conductivity.[86] To better observe the introduction of chemical bonding by modifying functional groups on the surface of nanoparticles, Zhang and colleagues introduced the chemical bonding by grafting poly(ether amine) (PEA) onto zinc hydroxyalkanoate (ZHS) as shown in (Fig. 4a). The modified nanoparticles were evenly dispersed collectively, providing tiny pores that were friendly to contact with the cathode material, which resulted

in excellent electrochemical stability of the material, as shown in (Fig. 4b). In a lithium plating stripping test at a constant current density of 0.2 mA cm^{-2} with a long-cycle stability of more than 1500 h and by testing the critical current (CCD), which reached 0.8 mA cm^{-2} as shown in (Fig. 4c), again demonstrating that the modified nanofillers of the functional group substantially improved electrochemical stability.[87]

Chen and colleagues incorporated zeolitic imidazolate framework-67 (ZIF-67) nanoparticles into $LiNi_{0.5}Co_{0.2}Mn_{0.3}O_2$ cells, resulting in a maintenance capacity of 123 mA h g^{-1} over 100 cycles at 1.0 C, through the active site of ZIF-67, the coordination of anions is restricted and the degree of dissociation degree of lithium salts is provided.[88] In a related investigation, Shen *et al.* demonstrated that the addition of ZIF-8 nanofillers can effectively decrease the interfacial impedance of ionic liquids through microporous physisorption, more effectively limiting the concentration of anions in the system, leading to improved cycling stability as shown in (Fig. 4d).[89]
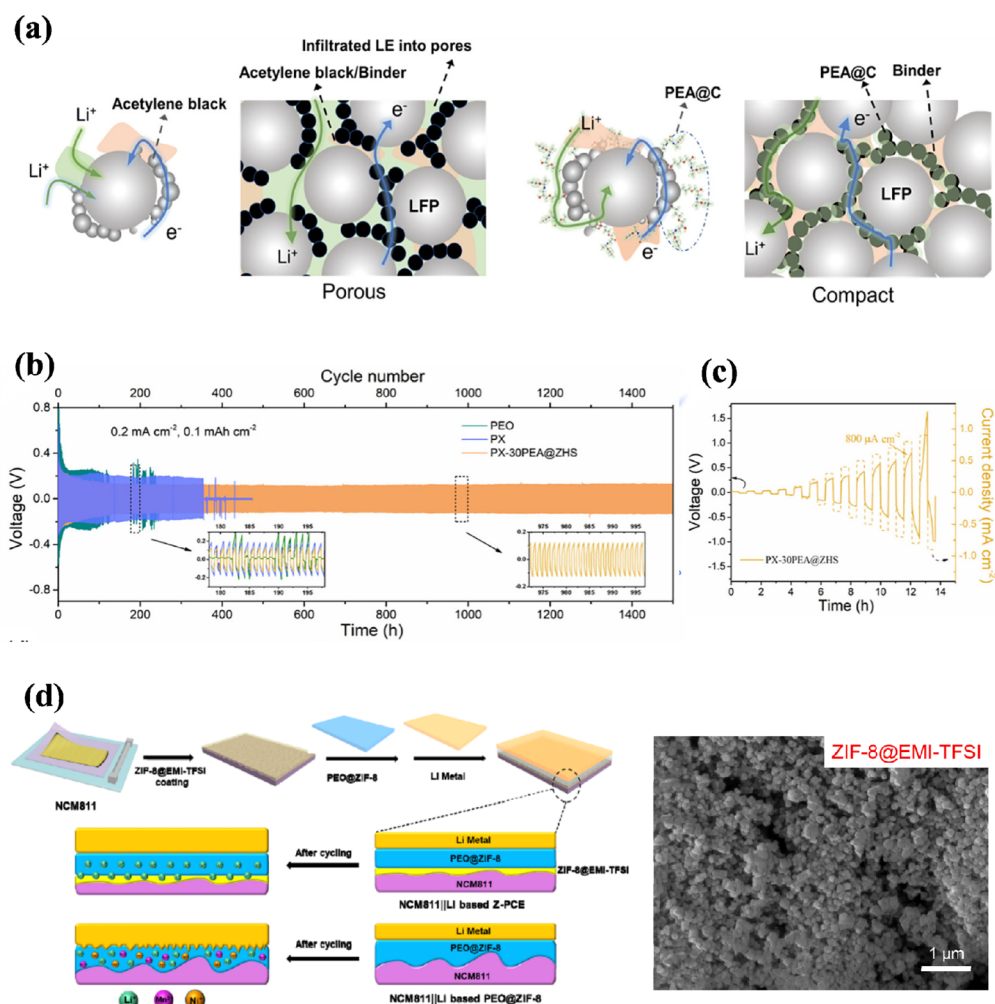
Fig. 4 (a) Schematic illustration of the traditional cathode with a porous configuration for electrolyte percolation, (b) Galvanostatic cycling of the symmetric cells with PEO, PX, and PX-30PEA@ZHS SPEs at 0.2 mA cm^{-2} with a capacity of 0.1 mA h cm^{-2}, (c) Galvanostatic cycling of the symmetric cells with PX-30PEA@ZHS SPEs at step-increased current densities ref. 87. Copyright 2022, Elsevier. (d) Schematic diagram of preparation and structure of NCM811/Li cell-based Z-PCE and PEO@ZIF-8 electrolytes ref. 89. Copyright 2022, Elsevier.

3.1.2 Nanofiber modifying SSEs. The utilization of 1-dimensional nanofillers, such as nanofibers and nanotubes, is prevalent in various applications. These nanomaterials can be integrated into the electrolyte to substantially improve the conductivity of lithium ions while also facilitating uninterrupted ion transportation.[90–95] Ferroelectric ceramics possess permanent dipoles that facilitate the movement of Li^+ ions by leveraging the electric field generated through self-polarization. This unique characteristic enables stronger Lewis acid–base interactions compared to nonferroelectric materials, thus improving the dissociation of lithium salts.[96–98] Kang and colleagues utilized electrostatic spinning and high-temperature calcination to produce porous ferroelectric material nanofibers (BIT), which were then incorporated as fillers into the PEO electrolyte. The pore structure of BIT nanofibers was found to decrease PEO crystallinity, leading to increased lithium ion migration with a conductivity of 6.25×10^{-4} S cm^{-1} at 50 °C (Fig. 5a). In addition, the piezoelectric characteristics of BITNF

promote a uniform distribution of ions, alleviate the accumulation of space charge and achieve the regulation of the dynamic balance at the organic–inorganic interface, resulting in excellent stability without any short circuit observed for up to 3000 hours in Li symmetric battery tests conducted at 50 °C.[99]

Nanotubes (NTs) have unique properties in the inner space and are added to the electrolyte as fillers, reducing interfacial circuitry and discontinuity, enabling both the surface and interior of the material to act as efficient channels for the fast movement of free lithium ions. As a result, not only does this enhance the mechanical strength of the PEO electrolyte, but it also facilitates the migration of lithium ions.

The presence of numerous oxygen vacancies on the surface of CeO_2, along with the addition of Ca, can enhance both the electrochemical and mechanical properties of the polymer. Chen *et al.* successfully synthesized hollow nanotubes enriched with vacant calcium in CeO_2 (Ca–CeO_2). The resulting structure facilitates a uniform lithium flux, as shown in
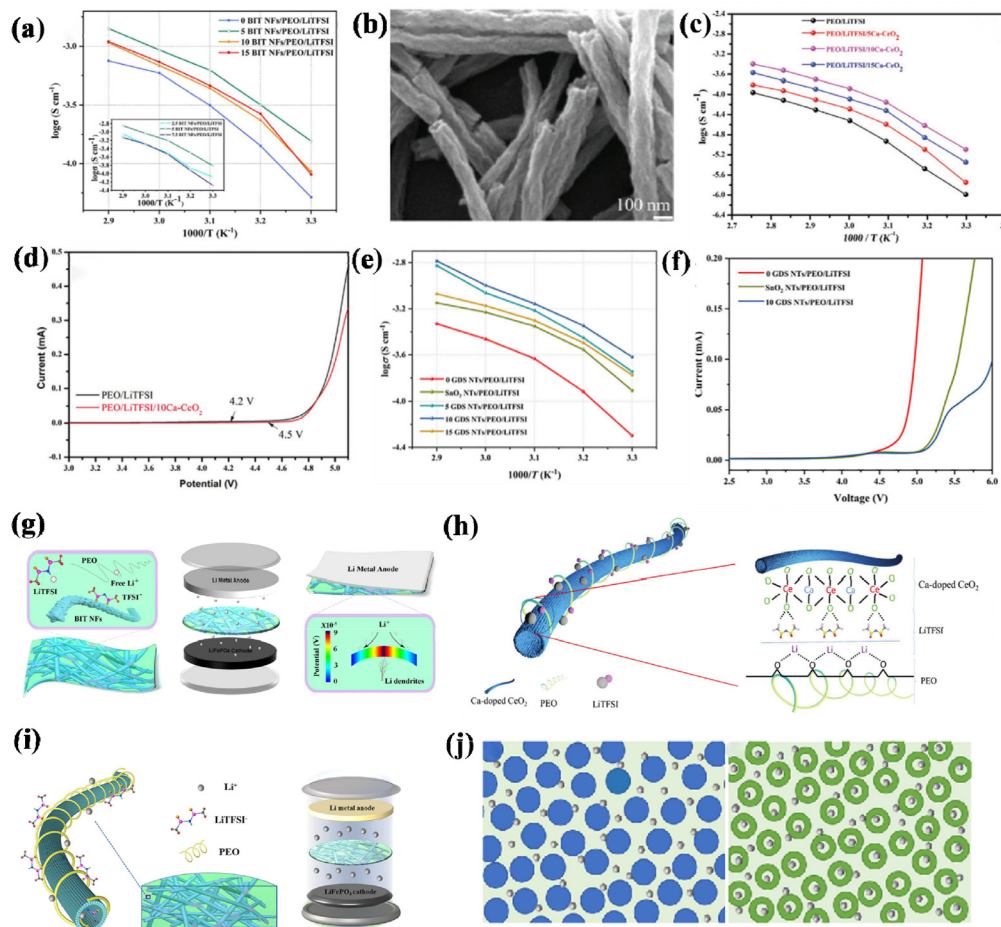
Fig. 5 (a) Arrhenius plots (temperature increased from 30 °C to 70 °C) ref. 99. Copyright 2022, Elsevier. (b) Characterization of Ca–CeO_2 SEM images, (c) Arrhenius plots of PEO/LiTFSI and PEO/LiTFSI/Ca–CeO_2 electrolytes, (d) LSV curves of PEO/LiTFSI and PEO/LiTFSI/Ca–CeO_2 films at a scanning rate of 1 mV s^{-1} at 60 °C (ref. 100). Copyright 2020, Wiley-VCH. (e) Arrhenius plots of several different electrolytes, (f) LSV curves of three different electrolytes ref. 101. Copyright 2023, Elsevier. (g) Schematic illustration of a mechanism for enhanced Li^+ ions transport and dynamic regulation of Li^+ ions deposition by BIT NFs ref. 99. Copyright 2022, Elsevier. (h) Schematic illustration of a mechanism for enhanced Li-ion transport in PEO-based electrolyte by Ca–CeO_2 nanotubes ref. 100. Copyright 2020, Wiley-VCH. (i) Mechanism for enhanced Li^+ transport by GDS NTs. (j) Comparison of the Li^+ transport path in the cross-sectional direction of nanofibers and nanotubes ref. 101. Copyright 2023, Elsevier.

(Fig. 5b), creating an efficient pathway for ion transport due to its larger contact area with the electrolyte. This leads to an impressive ionic conductivity of 1.33×10^{-4} S cm^{-1} at 60 °C, as demonstrated in (Fig. 5c). There is a positive correlation between the increase of oxygen vacancy and the ionic conductivity. Li^{+} cations move in the oxygen channel, accompanied by the change in coordination environment, starting from the process of ionic compounds being dissociated by polar solvent molecules and realizing rapid movement in the medium through the exchange of coordination molecules. To assess the ability to of the polymer electrolyte to withstand high voltages, linear scanning voltammetry (LSV) was performed at 60 °C using Li/SSE/SS cells to determine its electrochemical window, illustrated in (Fig. 5d). Interestingly, even under these conditions, the PEO/lithium bis(trifluoromethanesulfonyl)imide (LiTFSI)/Ca-CeO$_2$ electrolyte exhibits oxidative stability above 4.5 V, a crucial factor in further enhancing the theoretical capacity of SSEs.[100]

To further increase the oxygen vacancy, an electrolyte with good interfacial compatibility and excellent ionic conductivity was developed. Zhang *et al.* proposed the utilization of a Gd–SnO$_2$ nanotube filler to create long-range ion transport channels in PEO-based systems. This was achieved by taking advantage of its oxygen-rich vacancy mechanism, resulting in good interfacial compatibility and high ionic conductivity. When the positive charges carried by these oxygen vacancies were harnessed, Lewis acid sites were formed within the solid polymer, leading to strong interactions. Consequently, the composite electrolyte exhibited an elevated lithium ion conductivity of 2.41×10^{-4} S cm^{-1} at 30 °C (Fig. 5e). Furthermore, by combining the hollow structure with material modification techniques, there was a significant improvement in the enhancement of the electrochemical window (5 V), as shown in (Fig. 5f). In particular, this performance was close to that of commercially available liquid electrolytes.[101]

We explored the preparation of different one-dimensional nanomaterials (Fig. 5g–i) and compared the improvement of the polymer electrolyte performance by adding modified nanofibres and nanotube fillers, and found that nanofibres have a greater enhancement in mechanical strength, but the nanotube structure has a high specific surface while having a hollow structure to allow a uniform lithium flux, as shown in (Fig. 5j). Lithium ions can be transferred along the surface of the nanotube. At the same time, these particles quickly deembedded through the hollow transfer tube, which has a greater improvement on the ion transfer efficiency.

3.1.3 Nanolayer modifying SSEs. When Li^{+} is introduced into the cathode material to achieve charge equilibrium during periods of rest or movement,[102] the resistance to charge transfer (R_{ct}) increases as the solid electrolyte interface becomes thicker, leading to destabilization of the interface. To address this instability at the interface, Wang *et al.* developed interfacial nanolayers composed of aromatic amides (APA). The presence or absence of these nanolayers had a significant impact on the cycling stability of all-solid-state lithium batteries (ASSLBs), as shown in (Fig. 6a) and facilitated the rapid transport of lithium ions through steric channels within the nanolayer structure, as shown in (Fig. 6b). The initial charge/discharge profiles of NCM cathodes were examined in ASSLBs at a current density of 10 mA g^{-1}. The inset graph illustrates the initial coulombic efficiency and loss of energy density observed in ASSLBs. By analyzing the differences in capacity displayed in (Fig. 6c), it can be observed that there is a high overlap and good reversibility between the first two cycles on the curve cycle plot. This can be attributed to the reduced polarization achieved by constructing APA interfacial nanolayers, As (Fig. 6d) for the interfacial structure evolution, it shows the stability of the system, allowing repeated embedding and deembedding processes for lithium ions.[103] Using molecular engineering techniques to create this 2D nanostructure by binding organometal active sites, Xu *et al.* used molecular engineering techniques to design a nanosheet made of a 2-dimensional MOF. Using the electron-donating effect in its substituent, they aimed to enhance the number of ion mobility within PEO.[104] The preparation process depicted in (Fig. 6e) involves mixing metal salts with organic ligands in a solvent to produce a composite electrolyte consisting of these MOFs. This approach not only increases the available active sites but also offers valuable insights for the targeted design and simulation of Li ion transport within the complex electrolyte using DFT calculations, as illustrated in (Fig. 6f), effectively showcasing its internal stability.

As the two-dimensional layer structure prepared by the nanoframe itself can improve the mechanical strength of the solid electrolyte and promote the mobility of the polymer molecular chain, the perfect combination of matrix and filler can be realized; researchers used MXene as a filler to increase the amorphous region of the polymer.[105] Shi *et al.* explored sandwich-structured silica nanosheets (MXene–mSiO$_2$) with Lewis acid–base interaction depicted in (Fig. 6g), resulting in fast Li-ion transport at its interface and excellent resistance to deformation due to a Young's modulus of 10.5 MPa shown in (Fig. 6h). This can be attributed to the hydrogen bond between the rigid MXene–mSiO$_2$ nanosheets and the poly(propylene oxide) elastomer (ePPO) polymer matrix.[106] Furthermore, Zhang *et al.* improved the cycling stability of SSEs by incorporating a doped carbon–carbon composite transition metal carbide derived from the covalent organic framework (COF) and the 2D nitride MXene, along with the porous structure (CTT) and Mxene.[107] As a result, when paired with a solid electrolyte, the S@CTT/MXene cathode exhibited enhanced cycling performance compared to the prepared CTT and super-p as shown in (Fig. 6i). Ionic conductivity was measured as 1.64×10^{-4} S cm^{-1} at 80 °C according to (Fig. 6j), indicating solution homogenization and improved lithium-ion transport efficiency. It is worth noting that during the first 20 cycles, a lower capacity was observed in this battery based on (Fig. 6k). This could be attributed to the use of a solid-state electrolyte, which only contacts the surface of the cathode, unlike a liquid electrolyte that allows for full infiltration. Consequently, the incomplete reaction between the internal active substances initially leads to reduced capacity within these cycles.
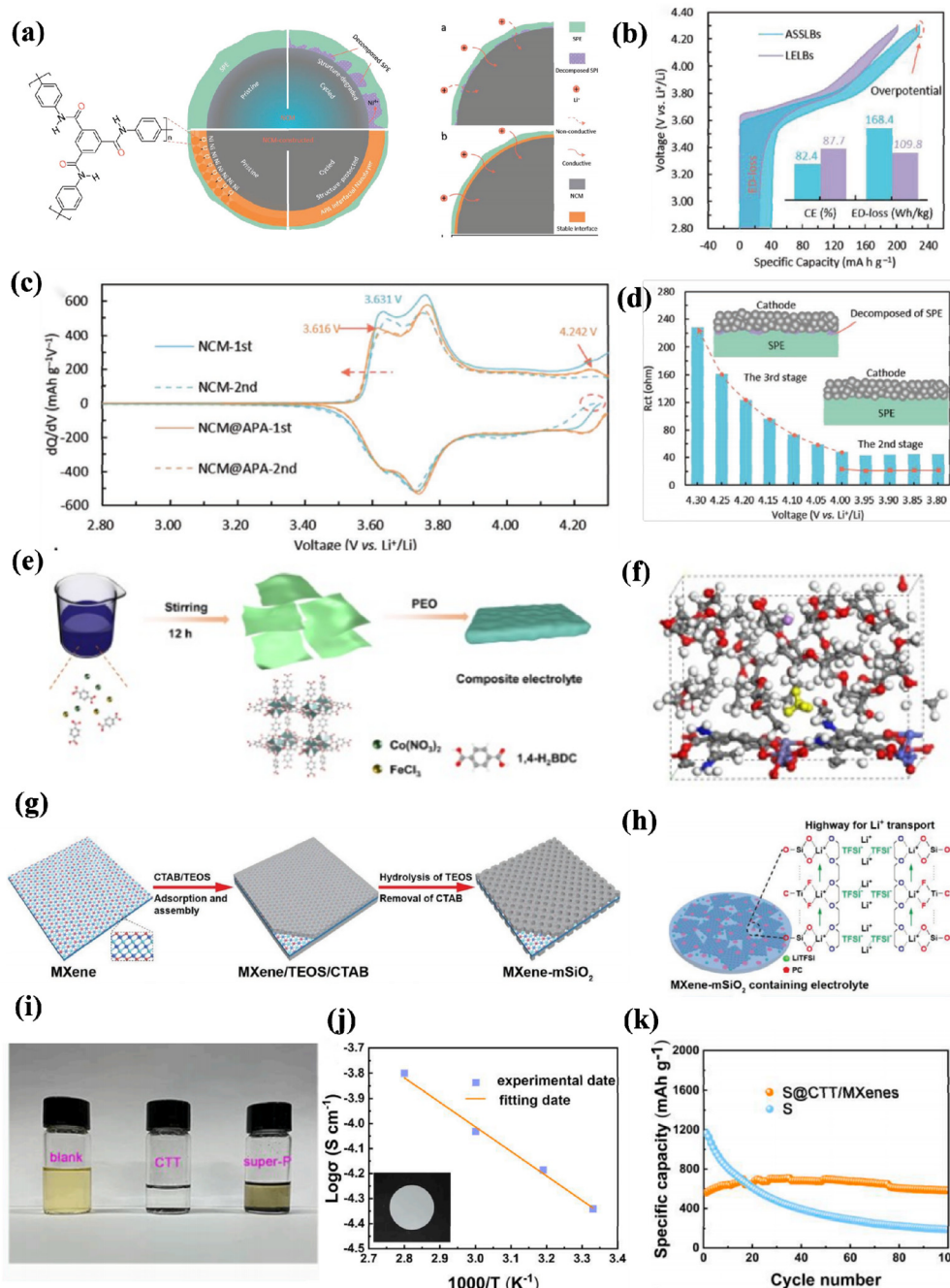
Fig. 6 (a) Schematic illustration of solid–solid interface without nanolayer and with APA interfacial nanolayer between NCM and SPE in affecting the cycling stability of ASSLBs, (b) the initial charge/discharge profiles of NCM cathodes in the ASSLBs under a current density of 10 mA g^{-1}, where the inset shows initial coulombic efficiency and energy density loss of the ASSLBs, (c) differential capacity curves of the 1st and 2nd cycle at 10 mA g^{-1}, (d) the evolution of R_{ct} in the NCM /SPE/Li ASSLBs during the initial charging ref. 103. Copyright 2022, Wiley-VCH. (e) Schematic diagram of the process for preparing MOFs and composite electrolyte membrane, (f) molecular dynamics simulation plots over time in the system of PEO/MOFs-NH$_2$ ref. 106. Copyright 2023, Wiley-VCH. (g) Schematic illustration of fabricating sandwich-like MXene-based mesoporous silica (MXene–mSiO$_2$) nanosheets, (h) schematic illustrating the fabrication of the MXene–mSiO$_2$ containing solid polymer electrolyte ref. 104. Copyright 2020, Wiley-VCH. (i) The optical images of Li$_2$S$_6$ solution before and after mixed with CTT and super-P, (j) ionic conductivity of PEO/PE solid electrolyte and the EIS plot of PEO solid electrolyte at 27 °C and 60 °C, (k) cycling performance at 200 mA g^{-1} (ref. 107). Copyright 2022, Elsevier.

However, the implementation of this design strategy significantly enhances the interface contact, thereby reducing the interface impedance considerably while ensuring more stable transportation of lithium ions. Using two-dimensional

materials in the solid electrolyte can form a hydrogen bond network with polymer chain segments and on the other hand, accelerate the dissociation of lithium salt through a local polarization electric field effect, which effectively inhibits den-

drites and side reactions, and achieve excellent cycling performance and significant service life.

3.1.4 Modifying the 3D skeleton structure of SSEs. To achieve a high-performance solid-state electrolyte, it is crucial to prevent the mutual agglomeration of fillers effectively. Therefore, it is essential to devise a three-dimensional framework for fillers that can provide composite SSEs with a high shear modulus, inhibiting the growth of lithium dendrites. Various methods such as the hydrogel method,[108–112] the template method,[113,114] and the 3D printing method have been used in the preparation of these fillers.[115] Wang *et al.* successfully used a template method to fabricate uniform porous 3D frames made of LATP, as depicted in (Fig. 7a). This involved using NaCl to form a three-dimensional structure, followed by washing to obtain a film with numerous random pores. The resulting film was then burned using an alcohol lamp, producing excellent thermal stability and safety, as shown in (Fig. 7g). Furthermore, when tested in a $LiFePO_4$(LFP)/(for the random LATP particles and PEO composite electrolytes) CPE-R/Li cell at a current density of 0.4 mA cm^{-2} for 600 hours (Fig. 7c), no significant presence of "dead Li" was observed on the surface of the Li anode from the results obtained. However, some roughness along with lithium dendrites was visible on the surface. This occurrence can be attributed to CPE-R containing a high filler content, which facilitates the rapid conduction of Li$^+$ ions through the interphase between the polymer matrix and fillers, but exhibits slower conduction within the polymer matrix. Therefore, the poor conductivity observed in Fig. 7b can be attributed to the formation of a discontinuous Li$^+$ conducting path due to the agglomeration of LATP particles. The integrated structure of (introduced into the 3D interconnected porous conductive framework of LATP to form CPE) CPE-3D plays an important role in inhibiting the growth of lithium dendrites by providing a continuous pathway for Li$^+$ conduction and having a high mechanical modulus.[116] Prepare high heat resistant SSEs according to the requirements of the use environment; Liu *et al.* also developed a composite electrolyte film based on PEO and 1-hexyl-3-methylimidazolium hexafluorophosphate (HMH) with improved stability and safety properties. The prepared film exhibits exceptional heat resistance, as demonstrated in (Fig. 7h), which shows its ability to maintain the stability of the lithium plating peel for an extended period of 250 hours. Furthermore, (Fig. 7f) illustrates that incorporating heat resistant fillers and constructing three-dimensional interconnection channels not only improves the heat resistance, but also improves the life of lithium-ion batteries.[117]

In order to pursue the ultimate safety of SSEs, there is no risk of burning, explosion *etc.*, in any case. The combination of aerogel makes it flame retardant, heat insulation, and has excellent electrochemical energy storage properties. This electrolyte utilizes aerogel as a carrier and absorbs ionic liquid or electrolyte into the aerogel to form a nonflowing solid electrolyte. It exhibits excellent performance under extreme conditions, such as high ionic conductivity at low temperatures. However, because it is a nonfluid solid electrolyte, it is suscep-

tible to polarization during high-current discharge, negatively impacting device performance. Lin *et al.* introduced rigid mesoporous silica aerogels as the framework for polymer-based electrolytes (Fig. 7e). This structure provides sites for anion adsorption, resulting in a high modulus of 0.43 Gpa (Fig. 7d) and an impressive ionic conductivity of $\approx 6 \times 10^{-4}$ S cm^{-1}, effectively inhibiting the growth of Li dendrites.[118]

More significantly, the multifunctional three-dimensional framework not only facilitates a continuous pathway for ion transport but also mitigates agglomeration and precipitation, thereby amplifying the synergistic effect of 3D framework formation and enhancing battery safety and stability.

In general, the incorporation of zero Vinamil particles into polymer-based solid electrolytes can facilitate polymer segment rearrangement, expand the amorphous region, and enhance ionic conductivity. However, addressing the issue of uneven diffusion remains challenging. One-dimensional materials (nanofibers, nanowires) and two-dimensional nanomaterials (nanosheets) possess non-continuous and tortuous ion transport channels that circumvent particle-induced "nodes" while facilitating the formation of high-quality continuous interfaces with polymers. Nevertheless, there is still a possibility of agglomeration. Therefore, to prevent isolated distribution of nano-fillers within the polymer matrix, it is necessary to establish a three-dimensional interconnected network for ion transport that effectively controls filler agglomeration and inhibits lithium dendrite formation. However, constructing solid electrolytes with such a three-dimensional framework is costly and complex; thus further exploration and improvement are required.

4. Polyester-based solid polymer electrolytes

Polyester-based solid-state polymeric electrolytes (SPEs) have received significant attention due to their robust polar functional groups [–O–(C=O)–O]. Notable examples include caprolactone (CL), ethylene ester (EC), and propylene carbonate (PC) (Table 1). These polyester electrolytes exhibit excellent compatibility with alkali metal salts, while their strong polar functional groups effectively enhance the dielectric constant and ionic conductivity of the electrolyte; linear block copolymers or grafted copolymers with various topologies are constructed to destroy the crystallinity of polyesters. Consequently, extensive research is being conducted to develop lithium-ion batteries base on high-performance polyester-based SPE.[119–122]
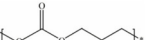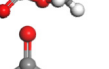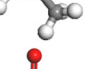
4.1. Solid polymer electrolytes (PCL)

The use of ε-caprolactone (PCL) in solid-state electrolytes (Fig. 8a) serves a dual purpose as a carrier and a matrix. PCL possesses specific structural properties that improve its ductility and mechanical strength, along with a relatively low glass transition temperature ($T_g < 60$ °C). Additionally, the weak interaction between the carbon group and lithium ions within PCL facilitates improved migration of lithium ions.[123,124]
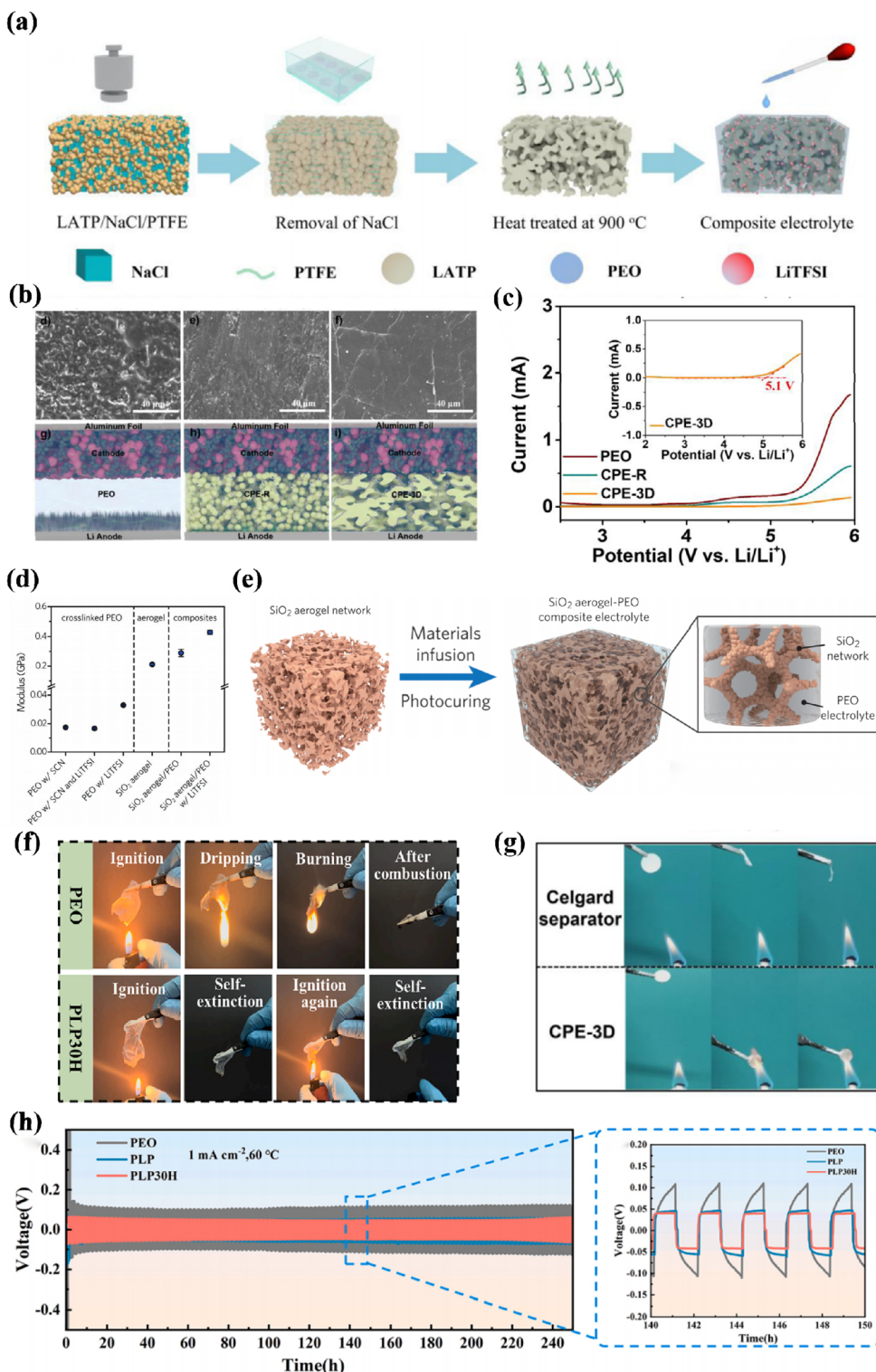
Fig. 7 (a) Schematic diagram of the fabrication of CPE-3D, (b) LFP/PEO/Li, LFP/CPE-R/Li, and LFP/CPE-3D/Li cells after charge/discharge cycling testes under 1 C, (c) voltage profiles of Li/PEO/Li, Li/CPE-R/Li, and Li/CPE-3D/Li symmetric batteries at different current density with 1 h stripping and 1 h alternating step ref. 108. Copyright 2022, Elsevier. (d) Elastic modulus of the crosslinked PEO, (e) schematic showing the synthetic procedures of the SiO$_2$-aerogel-reinforced CPE ref. 110. Copyright 2018, Elsevier. (f) The combustion behavior of SSEs ref. 109. Copyright 2023, Elsevier. (g) The combustion behavior of SSEs ref. 108. Copyright 2022, Elsevier. (h) Galvanostatic voltage test for Li−Li symmetric-cell for PEO (containing lithium salt), PLP, and PLP30H SSE (1 mA cm^{-2}) ref. 109. Copyright 2023, Elsevier.

Table 1 Properties of some typical polyester–based solid polymer electrolytes

Polymer	Chemical structure	Molecular model	T_g (°C)	T_m
PCL			−60	Amorphous
PEC			5	Amorphous
PPC			35	Amorphous
PTMC			−16	Amorphous
PCL-PTMC		—	−28	Amorphous

Mindemark *et al.* initially developed a solid-state electrolyte using PCL material; however, its high crystallinity at room temperature limited its potential applications.[125] To address this issue, Zhang and colleagues introduced inorganic fillers to facilitate Li^+ transport within the electrolyte matrix. By incorporating 45 wt% LiTFSI and 75% LAGP into PCL, they achieved an impressive ionic conductivity of approximately 1.75×10^{-4} S cm^{-1} at a temperature of 30 °C (as depicted in Fig. 8b). Furthermore, the introduction of LAGP into the electrolyte demonstrated improved compatibility between the PCL and the Li anode during lithium plating stripping tests conducted over multiple cycles. This enhancement did not compromise the mechanical properties of the electrolyte (Fig. 8c).[126] Sångeland *et al.* successfully inhibited PCL crystallization by incorporating bis(methylene carbonate) (TMC), leading to substantial improvements in cell performance. They also discussed the deposition of interfacial by-products and the growth of lithium dendrites (Fig. 8g), which resulted in a reduced interfacial impedance. Additionally, three cycles of Open Circuit Voltage (OCV) to −0.5 V and OCV to 5 V were performed to observe irreversible interfacial species build-up during reduction and oxidation, respectively (Fig. 8f).[127] To study the interfacial contact, Chen *et al.* developed a poly (ether-ester)-based poly(pyrrolidone chloride) (PDCL-SPE) with adjustable composition and structure through direct bulk of cyclic monomers CL and poly(1,5-dioxepan-2-one) (PDXO). The amorphous structure, lower glass transition temperature, as well as synergistic effects from the ether and carbonyl groups facilitated the dissociation of lithium salts and transport of lithium ions even after long-term cycling (600 h). The charge/discharge voltage curves for Li/PDCL40-SPE/Li remained stable with a low polarization potential (0.04 V).[128] P. Nkosi *et al.* added LLZO at different levels to improve composite electrolyte performance with LiFePO$_4$ cathode interfacial contact, achieving a conductivity value of 1.31×10^{-4} S cm^{-1} at 60 °C (Fig. 8d). This was attributed to the formation of random connectivity among ceramic particles, as well as long-range connectivity at the polymer–ceramic interface (Fig. 8e).[129] Since the conductivity of PCL is an order of magnitude larger than that of PEO-based "ceramic polymers", the introduction of ceramic particles does not reduce ionic conductivity, has excellent interfacial contact, and has stable electrochemical performance at 5 V voltage, offering prospects for the production of high energy-density solid lithium batteries.

4.2. Solid polymer electrolytes (PEC)

An EC is a member of the aliphatic group, and research has indicated that the aliphatic backbone possesses enhanced flexibility, allowing for more frequent movement of chain segments. Its synthesis involves the copolymerization of carbon dioxide and epoxide.[130–133] Additionally, its thermodynamic stability can be attributed to its five-membered ring structure. Elmér *et al.* conducted a study on the coordination behavior of Li^+ in the PEC/LiClO$_4$ system using Fourier infrared (FTIR) spectroscopy, the concentration of lithium ions increased by decreasing solvent polarization.[134]

PEC, as a low-donor-concentration molecule, can reduce the coordinate bonding between the polymer chains and lithium ions in the polymer framework, thus increasing the ionic conductivity. Wang and his team successfully developed a new solid polymer electrolyte by incorporating a carbonate substrate with a unique functional group (4-vinyltrifluorotoluene) through a precise molecular design, as shown in (Fig. 9a). This non-covalent bonding effect greatly enhances lithium ion migration and can also be used as a composite cathode bonding agent, leading to improved active mass loading and
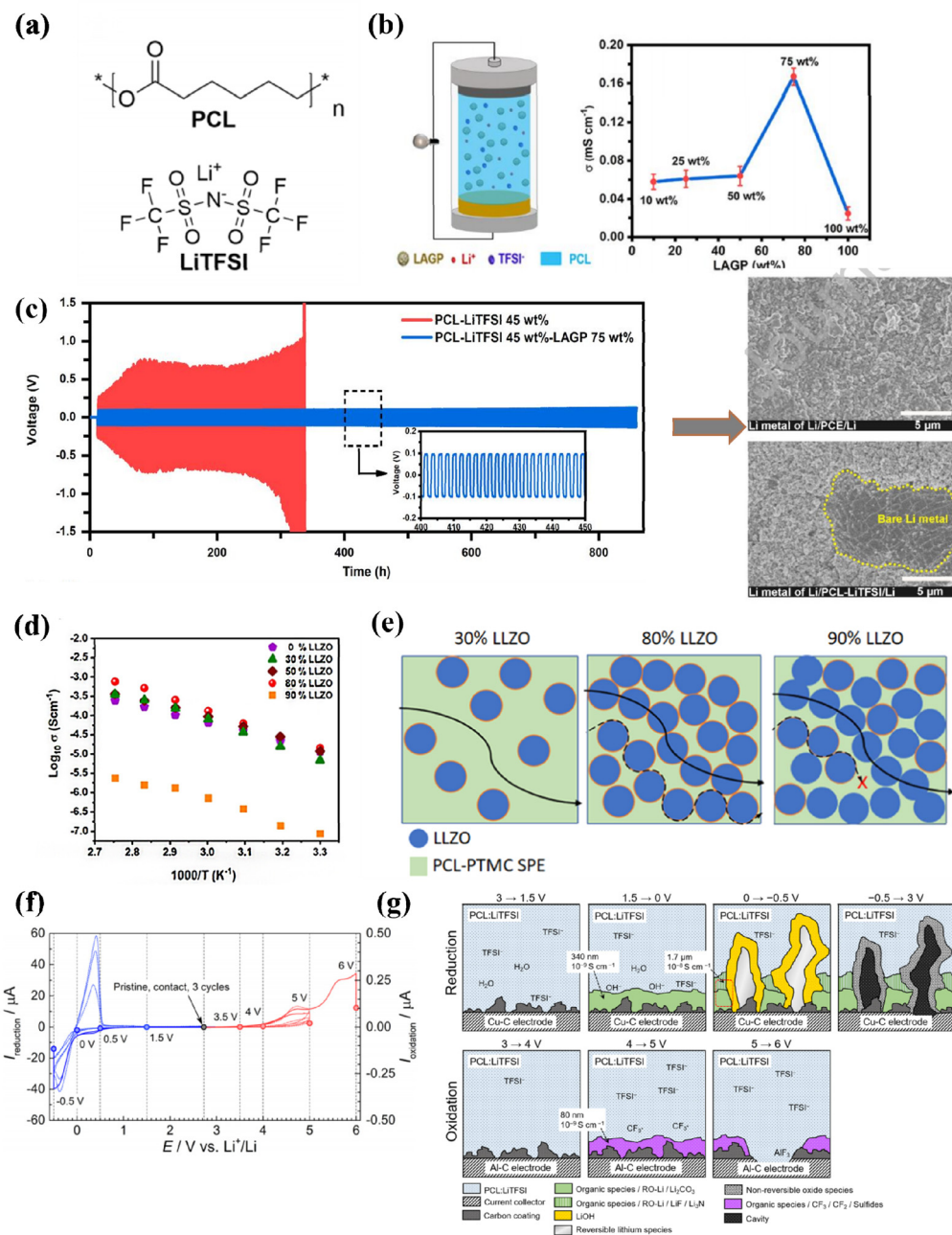
Fig. 8 (a) Structure of poly(ε-caprolactone) ref. 127. Copyright 2015, Elsevier. (b) Ionic conductivity of the composite electrolyte, (c) Galvanostatic tests of Li/PCL-LITFSI 45 wt%-LAGP 75 wt% Li and Li/PCL-LiTFSI 45 wt% Li cells at a constant current density of 0.1 mA cm^{-2} (ref. 126). Copyright 2021, Elsevier. (d) Comparison of Arrhenius plots for the ionic conductivity of the polymer and composite electrolytes with different LLZO loadings, (e) schematic representation of the Li-ion transport in composite electrolytes at 30 wt% LLZO, 80 wt% LLZO, and 90 wt% LLZO loadings ref. 129. Copyright 2021, Elsevier. (f) Current profiles of Li/PCL: LiTFSI/Cu–C or Al–C cells taken apart for postmortem morphological and compositional analysis, current response during linear sweep to different cutoff potentials followed by a potential hold for 3 h (solid line) and during the first three cycles, (g) schematic of solid polymer electrolyte–electrode interface at different potentials. Interfacial layer thickness and ionic conductivity are based on calculations that assume that the interfacial layer covers 50% of the electrode area ref. 127. Copyright 2015, Elsevier.

enhanced interfacial chemical stability.[135] It is worth noting that the impact of anion conduction on lithium ion mobility is mainly based on the receptor chain segment within the polymer matrix, as illustrated in (Fig. 9b). The molecular orbital HOMO and LUMO energy levels are depicted, providing further information on the chemical structure of this modified fluorinated polymer electrolyte (MFPE) in (Fig. 9c). To achieve a wider electrochemical window, higher-energy bands are required. This phenomenon explains why there exists such a strong interaction between polymer-incorporated lithium salts.[136]
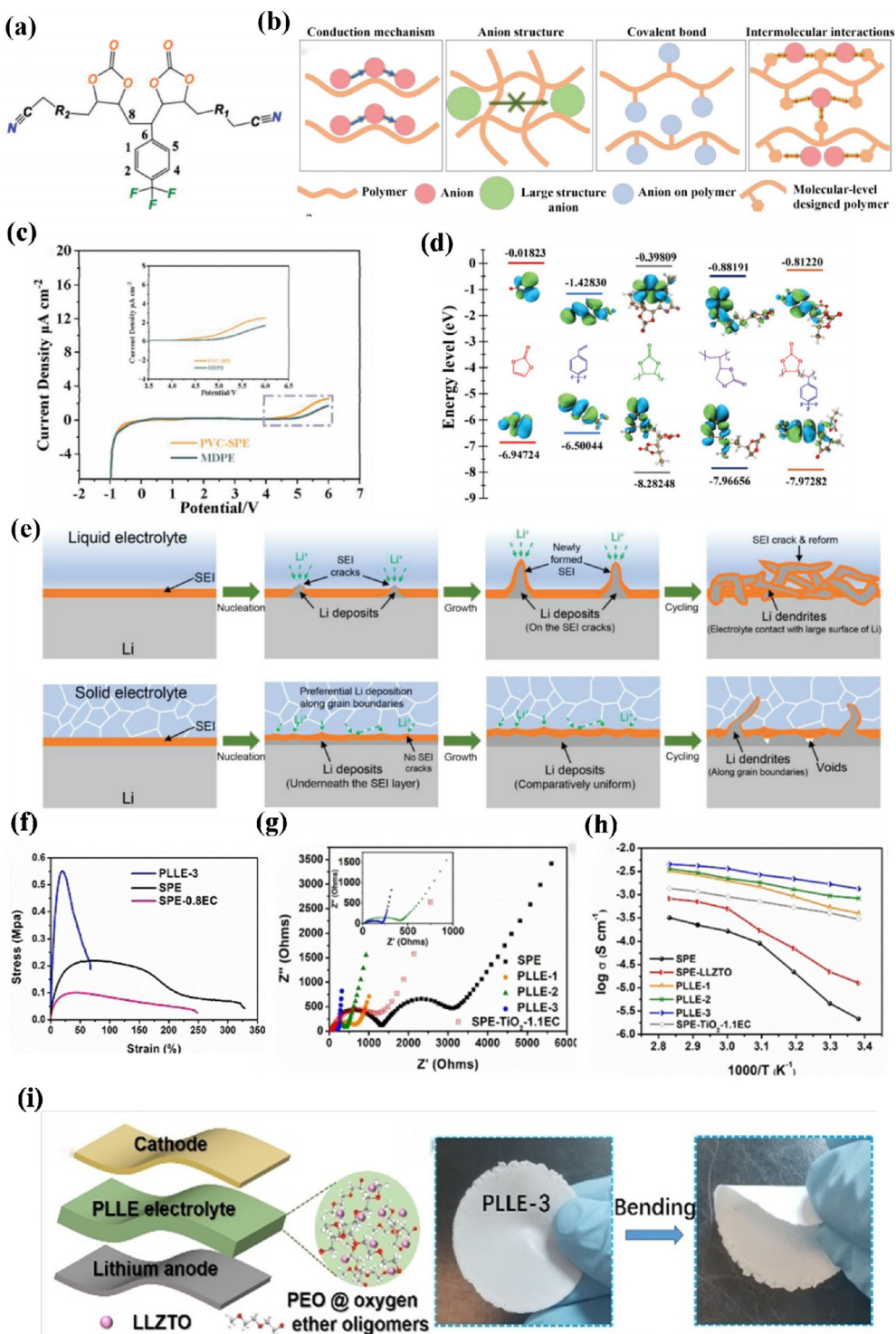
Fig. 9 (a) Schematic of novel molecular-level designed polymer structures, (b) scheme of conduction mechanism of anion in polymer and different separate measures of increase lithium-ion transport, (c) linear voltammetry curve of Li/PVC-SPE/SS and Li/MDPE/SS, (d) the HOMO and LUMO of Vinyl Chloride (VC), PVC unit, poly(vinyl ethylene carbonate) ref. 127. Copyright 2023, Wiley-VCH. (e) Schematic illustration of Li deposition behavior in liquid electrolytes and schematic illustration of Li deposition behavior in solid-state electrolytes ref. 128. Copyright 2023, Wiley-VCH. (f) H NMR spectra showing EC structural changes under the influence of LLZTO, (g) impedance spectra of Li/SPE or SCEs/LiFeO$_4$ cells, (h) Arrhenius plots of PEO and its composite electrolytes, (i) composite electrolyte (PLLE) ref. 131. Copyright 2021, German Chemical Society.

To improve the ionic conductivity of solid electrolytes and reach a level of that of liquid electrolytes, we incorporated an additive called ethylene carbonate (EC). Liu *et al.* devised a method to enhance the interaction between active $Li_{6.4}La_3Zr_{1.4}Ta_{0.6}O_{12}$ (LLZTO) doped with EC and Ta using PEO and LiTFSI (PLLE), resulting in a composite electrolyte with an ionic conductivity of 1.43×10^{-3} S cm^{-1} at 25 °C (Fig. 9g). The inclusion of EC had a synergistic effect by reducing the crystallinity of PEO while also acting as a plasticizer compared to other SSEs doped with LLZTO, thus maintaining a higher ion transport efficiency (Fig. 9h). Compared to liquid electrolytes and PLLE, it is evident that PLLE demonstrates better inhibition against lithium dendrites due to the formation of a solid electrolyte interfacial layer on its surface through vinyl carbonate decomposition (Fig. 9e).[137] Cyclic monomers are widely recognized to undergo decomposition when exposed to Lewis acids or bases as initiators.[138] Therefore, we propose that at high temperatures (>100 °C), there is an interaction between EC and LLZTO that triggers ring-opening reactions in the reactive structural state of EC based on the findings of our tests using 1H NRM (Fig. 9f).[139]

4.3. Solid polymer electrolytes (PPC)

Propylene carbonate (PPC) exhibits excellent resistance oxidation and demonstrates stable cycling performance at high voltage, offering an electrochemical window of 4.6 V.[140–144] Moreover, PPC is readily dissolvent in a wide range of organic solvents. However, its mechanical properties are relatively poor. To address this limitation, Cui *et al.* investigated PPC-based SSEs and successfully developed LFP batteries with enhanced capacity within the temperature range of 0–160 °C. In another study by Chen *et al.*, a composite electrolyte composed of PPC/LZTO was designed, incorporating inorganic fillers to modify the rate capacity and cycling stability of PPC.[145]

The stable SEI interface formed by the PPC-based solid electrolyte is a key factor for the long-cycle stability of lithium batteries. Jia and his colleagues conducted a study on the chemical decomposition pathway of PPC to alkaline LLZTO particles to investigate (Fig. 10a). According to the literature, when hydroxide and glycerol are present along with alkali and water, PPC decomposes into cyclic propylene carbonate (PC). In (Fig. 10b), different temperatures were used for the EIS analysis of PPC.[146] Sung *et al.*, on the other hand, incorporated LAGP as an active filler into the propylene carbonate matrix, which exhibited good compatibility with the lithium metal as shown in (Fig. 10e). Additionally, the LAGP particles showed favorable wettability with PPC as illustrated in (Fig. 10c). The optimization of the performance of this composite electrolyte was evaluated using different LAGP contents represented by (Fig. 10g). Interestingly, the LFP/PPC-LAGP/Li cell achieved an impressive discharge specific capacity of 50 mA h g^{-1} with 63% capacity retention over 1000 cycles and nearly 100% crossover efficiency, as shown in (Fig. 10f). These outstanding results indicate that, compared to the LFP cathode, PPC-LAGP also exhibits exceptional stability at high currents.[147] To enhance the thermal stability of batteries, Luo *et al.* introduced a polyimide (PI)-PPC substrate doped with LLZTO as reported in the literature. This resulted in an excellent thermal stability of the composite electrolyte. XRM analysis demonstrated that the LLZTO filler was evenly distributed within the matrix shown in (Fig. 10d), this rational doping reduces the agglomeration phenomenon, makes lithium deposition uniform, and reduces lithium dendrites puncture.[148]

The addition of active filler can substantially improve lithium-ion transport capacity, but still needs to improve its interface engineering, Wang *et al.* designed a bilayer solid polymer by putting polypropylene carbonate (PPC)/succinonitrile (SN) in contact with the cathode (DSPE), while the anode uses PEO/LiLa$_3$Zr$_2$O$_{12}$, and for further study of the interaction diagram of PPC, PEO, SN, PPC (Fig. 10h) synergizes stronger with PEO than PEO, so this structure has a high critical current density of 1.3 mA cm^{-2}, the onset decomposition potential of DSPE at 25 °C is 5.6 V, which proves its excellent electrochemical performance.[149]

5. Nitrile-based solid polymer electrolytes

Nitriles, which possess the NC group that is polar in nature and electron-withdrawing, exhibit high dielectric constants of approximately (ε = 30). Their wide electrochemical window may be attributed to their low LUMO energy. Recently, there has been significant interest in nitrile-based SPEs due to their excellent electrochemical properties and strong coordination capabilities.[150–153]

5.1. Butylene dinitrile solid polymer electrolytes

The plastic phase of succinonitrile (N–C–CH$_2$–CH$_2$–N, SN) spans from −35 °C to its melting point at 62 °C, with a boiling point of 265 °C. At 25 °C, the dielectric constant (ε = 55) of SN was measured, indicating its strong solvent capabilities for various lithium salts. The high oxidation potential of SN can be attributed to its ability to accept electrons due to the lower LUMO energy level.[154]

It is widely acknowledged that SN-based solid electrolytes with oxidation resistance exhibit good compatibility with high-voltage electrode materials. However, the presence of residual SN molecules, while capable of reducing the interfacial impedance by infiltrating the cathode material, also poses a risk of corroding the lithium–metal anode. To enhance the connection with the high-voltage cathode, Zuo and colleagues have implemented an *in situ* curing process between PEO and the cathode by introducing SN plastic crystals in between. This approach forms an ion-conducting network within the cathode and at its interface, as shown in (Fig. 11a), effectively preventing the oxidative decomposition of PEO during high-voltage charging and discharging. As a result, they were able to extend the electrochemical window to 5.2 V (as depicted in Fig. 11b), demonstrating excellent electrochemical stability.[155]
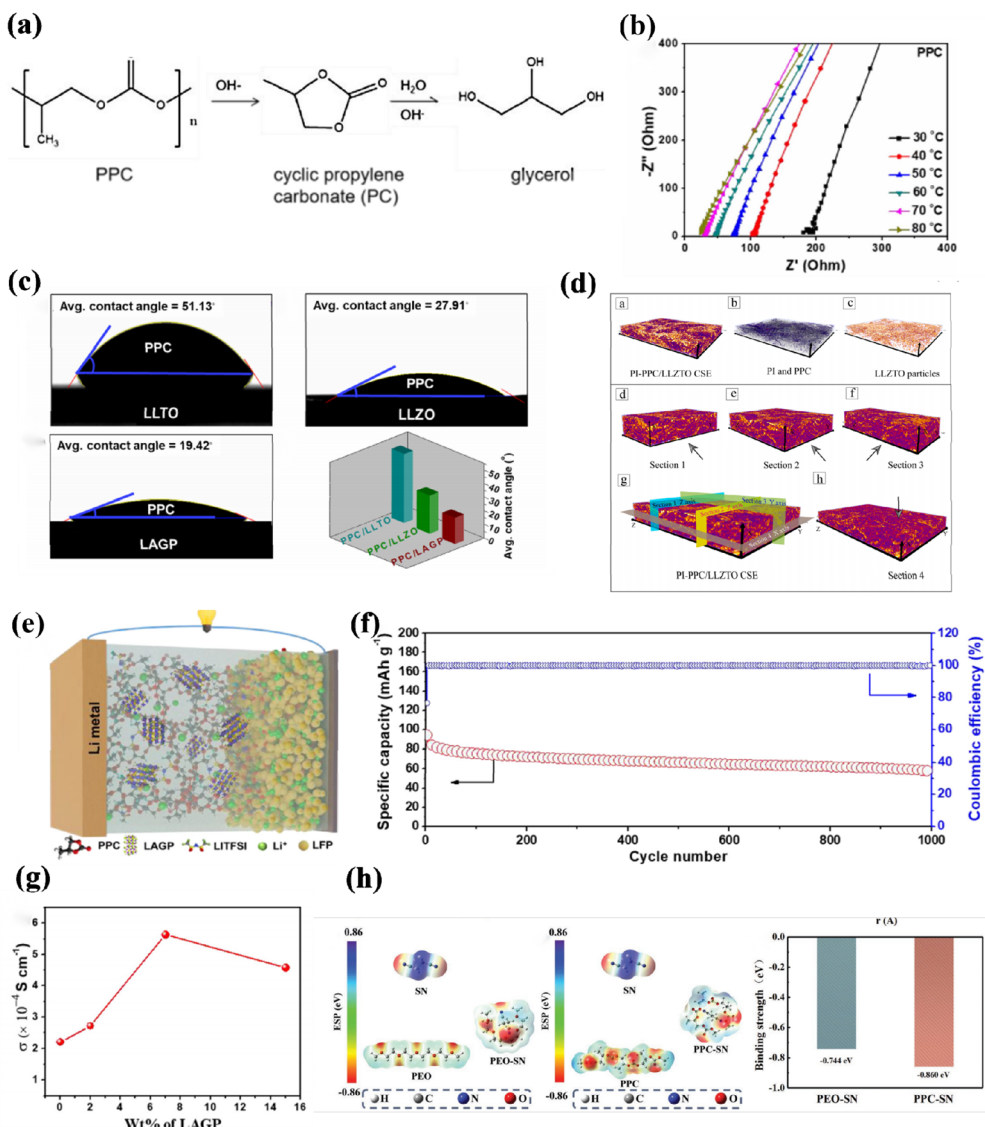
Fig. 10 (a) Possible chemical decomposition pathways of PPC against the LLZTO particles, (b) Nyquist plots of PPC at various temperatures ref. 146. Copyright 2020, American Chemical Society. (c) Histogram of average contact angle for comparison among PPC and LLTO, LLZO, and LAGP ref. 147. Copyright 2021, Elsevier. (d) 3D XRM analysis of PI-PPC/LLZTO SPEs ref. 148. Copyright 2021, Elsevier. (e) Schematic of a LFP/PPC–LAGP/Li full cell, (f) corresponding cyclability at 60 °C, (g) LSV curve of DSPE at 25 °C ref. 147. (h) Optimized geometrical configurations and calculated potential potentials were used to obtain the optimal configurations of PEO-SN and PPC-SN and to calculate their binding energies ref. 149. Copyright 2023, Wiley-VCH.

In order to enhance the overall performance of cells, the bilayer structure can be utilized. Additionally, the stability at the interface between SN and lithium metal anodes can be improved by incorporating double salts or suitable additives such as fluoroethylene carbonate (FEC). Bao *et al.* proposed a simple method of phase separation using SN to modulate the preparation of porous membranes made from poly(vinylidene fluoride-*co*-hexafluoropropylene) (PVDF-HFP) (SPH). They employed a double salt system consisting of LiTFSI and lithium bis(oxalate)borate (LiBOB) to provide Li$^+$ ions (DPCE) (Fig. 11c). In contrast, the dense pore structure of SPH20 plays a crucial role in impeding dendrite growth during this process. Furthermore, continuous plating/stripping oper-

ations were maintained for more than 1200 hours in the case of the Li|SPH20-DPCE|Li cell (Fig. 11d). The resulting ionic conductivity at room temperature reached 8.21×10^{-4} S cm^{-1} (Fig. 11e). Consequently, when assembling a LFP/SPH20-DPCE/Li cell, it exhibited superior cycling stability compared to pure PVDF-HFP and commercially available glass fiber materials. This led to a relatively smooth surface morphology for the Li–metal electrode. When identical DPCE is used employed in two symmetric lithium cells, it can be concluded that the loose and brittle fiber structure of GF would inevitably facilitate dendrite growth during the plating/stripping process of lithium deposition/dissolution as shown in (Fig. 11d).[156]
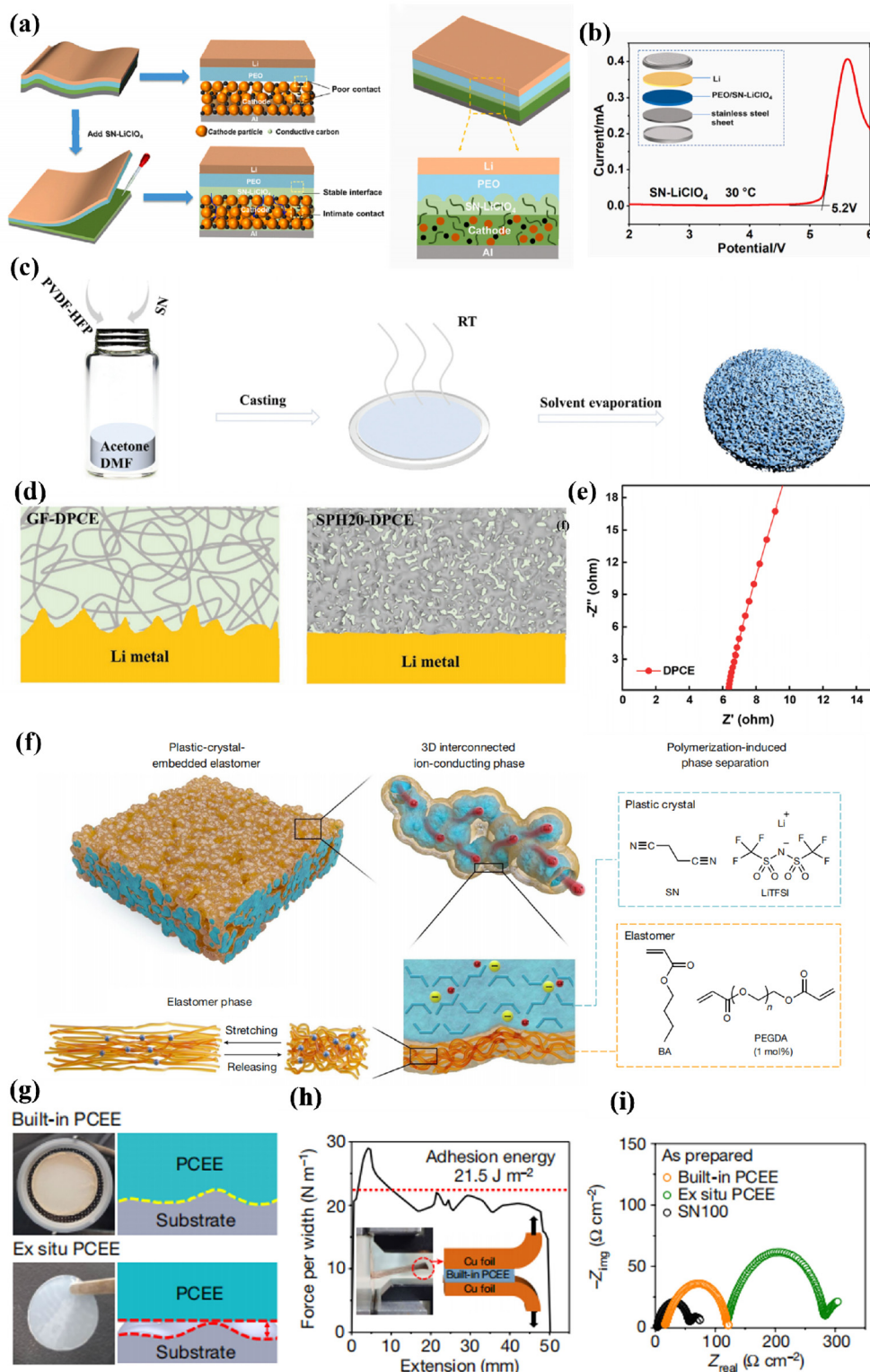
Fig. 11 (a) Schematic diagram of NCM/PEO/Li cells with interfacial modification layer, (b) LSV curve of PEO/SN-LiClO₄ ref. 155. Copyright 2023, Elsevier. (c) Schematic illustration of the fabrication process of porous polymer host, (d) schematic diagrams of Li deposition in Li/Li cells assembled with GF-DPCE and eSPH20-DPCE, (e) DPCE EIS impedance mapping ref. 156. Copyright 2023, Wiley-VCH. (f) Schematic illustration of the design and structure for PCEE. The structure of PCEE shows that the 3D interconnected plastic crystal phase (cyan) is surrounded by the elastomer phase (orange), (g) photo images and schemes showing the *ex situ* and the built-in PCEEs, (h) interfacial adhesion test between the built-in PCEE and the Cu foil. (i) Nyquist plots of as-prepared symmetric Li cells configured with various electrolytes ref. 157. Copyright 2023, Springer Nature.

The dispersion function component of elastomers, such as SN, has been found to exhibit excellent properties in terms of its ability to disperse materials effectively. Lee *et al.* have reported on a group of solid-state electrolytes made from elastomers that possess a three-dimensional interconnected plastic crystal phase (PCEE). These elastomeric electrolytes demonstrate a combination of mechanical strength, high conductivity for ions, low resistance at interfaces, and a high transference number for lithium ions (Fig. 11f). The *in situ* generated elastomer electrolyte on copper foils effectively accommodates volume changes during prolonged lithium plating and stripping processes, achieving a remarkable coulombic efficiency of 100%. Furthermore, these elastomer electrolytes enable stable operation of full cells even under constrained conditions such as limited lithium availability, thin electrolyte layers, and high-loading $LiNi_{0.83}Mn_{0.06}Co_{0.11}O_2$ cathodes operating at a high voltage of 4.5 V at room temperature. By establishing uniform ion transport channels, the impedance is significantly reduced, resulting in a high specific energy exceeding watt hours per kilogram of electrode plus electrolyte, while effectively preventing the formation of lithium dendrites (Fig. 11g). The implementation of an elastomeric electrolyte system presents a robust approach to ensure the stable performance of high-energy solid state lithium batteries.[157] Furthermore, (Fig. 11h) shows an impressive adhesion energy value of 21.5 J m^{-2} for this system that surpasses that observed in most commercially available polymer electrolytes, thus showing excellent interfacial stability (adhesion energy greater than or equal to 5 J m^{-2} is considered crucial to create durable interfaces capable of withstand mechanical stresses associated with battery manufacturing and operation).[158]

5.2 Solid polyacrylonitrile electrolytes

The PAN is formed through the polymerization of acrylonitrile monomer radicals and exhibits excellent thermal stability. It lacks oxygen atoms, and the nitrogen atom in PAN does not strongly interact with lithium ions. Its ionic conductivity can reach 3 mS cm^{-1} while possessing an electrochemical window exceeding 4.5 V.[159–163] However, due to its low strength and poor mechanical properties, PAN has been used predominantly utilized as a gel polymer electrolyte (GPE) for a long period.[164]

This is primarily attributed to uncontrolled passivation reactions that occur between the nitrile group and the lithium-metal anode, resulting in increased interfacial resistance between the electrolyte and electrode, which deteriorates electrochemical performance. Consequently, PAN alone is not suitable for polymer electrolyte-based materials.[165]

To enhance the stability at the interface, we incorporated PAN fibers into a three-dimensional structure. This structural modification greatly improved the overall performance of the solid electrolyte and facilitated stable long-term cycling.[166] In order to address the low activity and ionization ability of MOFs in electrochemical reactions, Zhang *et al.* introduced ionic liquids (IL) to enhance their activity. When efficient ionic liquids are incorporated, Li$^+$ ions are transported along the chain of MOFs rather than through conduction at the interface. The preparation process is depicted in (Fig. 12a). In particular, the MOF@PAN/PEO/IL composite exhibits an impressive ionic conductivity of 2.57×10^{-4} S cm^{-1} at 25 °C (Fig. 12b), which is two orders of magnitude higher than other composites used as solid-state LMB operating at room temperature (RT). The stability test shown in (Fig. 12c), conducted for 600 hours with repeated lithium plating and stripping cycles, demonstrates that densely packed MOF nanoparticles grown on PAN fibers form continuous pathways for Li$^+$ transport. Furthermore, the encapsulating of an ionic liquid (IL) within MOFs not only reduces energy barriers for fast Li$^+$ migration but also enhances the interfacial compatibility between various MOF/PEO and electrode/electrolyte interfaces.[167]

Polyacrylonitrile nanofiber mesh with a strong three-dimensional skeleton can provide support for the ionic conductive matrix and significantly improve the overall mechanical properties. Bandyopadhyay *et al.* has reported the synthesis of a unique one oligomer of type A–B–A–B from a diamine, 1,4-diazabicyclo [2.2.2] octane dihalide diethylene glycol bis (2 chloroethyl) ether, with three units of oxyethylene (–CH$_2$CH$_2$O–) in the backbone through the Menschutkin reaction. Subsequently, this oligomer was blended with PAN and subjected to heat treatment to form a vein-like network structure. In this structure, PAN serves both as a supporting skeleton and as a pathway for lithium-ion transport. This innovative approach provides an alternative design strategy for the preparation of high-performance pan-based electrolytes.[168] To bind the active site of organometallic particles and make them have good dispersion. Li and his team took an innovative approach by creating a connected three-dimensional network structure using MOFs, effectively establishing continuous channels for rapid transport of Li$^+$ ions within the MOF particles (Fig. 12e). Among the commonly used MOF particles (Fig. 12d), the université Catholique de Louvain-66 (UIO-66) exhibits superior porosity and anion adsorption energy, thus limiting anion transport in the cell while improving the number of lithium ion transfer (t_{Li^+}). The ionic conductivity, mechanical properties, and electrochemical stability of uio-66 are significantly better than other 3D polymer electrolyte frameworks (Fig. 12f–h). Simulation results also demonstrate a uniform distribution of lithium flux throughout (Fig. 12d), dendrite formation due to effective modulation of the 3D framework structure that restricts anion transportation.[169] In terms of the SEI interface (as depicted in Fig. 12i), dense LiF/Li$_3$ formation promotes efficient transfer kinetics for Li$^+$ ions and improves the overall stability of the structural system, ultimately prolonging the useful life of solid-state Li-ion batteries.[170]

6. Polyvinylidene difluoride-based solid polymer electrolytes

PVDF is a partially crystalline polar polymer that displays a high dielectric constant, which enhances the interaction
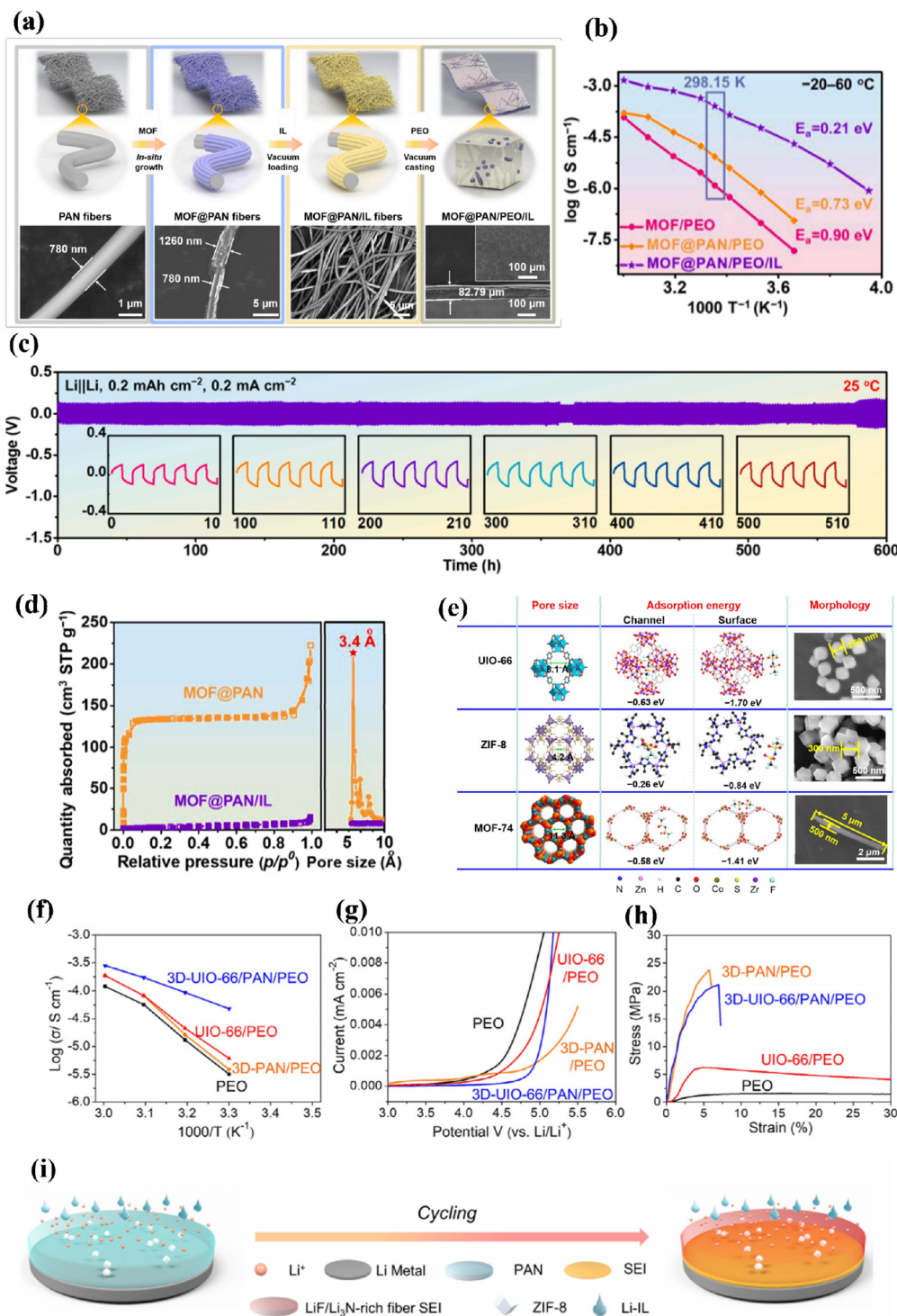
Fig. 12 (a) Schematic diagram of the fabrication process of the MOF@PAN/PEO/IL CPE and their corresponding SEM images. (b) Ionic conductivity of different CPEs as well as their activation energy at the temperature range of 20–60 °C. (c) Long-term cycling stabilities of Li/Li symmetric cell using MOF@PAN/PEO/IL CPE at a current density of 0.2 mA cm^{-2} for 0.2 mA h cm^{-2}. (d) Li$^+$ distributions in MOF@PAN/PEO/IL CPE at pristine (0 s), intermediate (60 s), and steady (10 h) ref. 167. Copyright 2022, Elsevier. (e) The crystalline structures and SEM images of UIO-66, ZIF-8, and MOF-74, clearly show their differences in pore sizes, adsorption energies with TFSI$^-$, and morphologies. (f) Temperature-dependent ionic conductivities. (g) Oxidative stabilities ref. 169. (h) Stress−strain curves of the PEO/LiTFSI, 3D-PAN/PEO/LiTFSI, UIO-66/PEO/LiTFSI and 3D-UIO-66/PAN/PEO/LiTFSI SSEs ref. 169. Copyright 2022, Elsevier. (i) Schematic drawing of suppressing Li dendrites ref. 170. Copyright 2023, Wiley-VCH.

between the matrix and lithium salts to speed up their dissolution and transmission of Li$^+$ ions. Furthermore, PVDF has excellent heat resistance and mechanical deformation resistance, along with outstanding compatibility at the interfaces. These properties have recently made PVDF an attractive option for solid polymer electrolytes in extensive research studies.[170–173]

To develop a flexible all-solid-state lithium metal battery with a high-density three-dimensional structure, Wang *et al.* utilized PVDF as a supporting framework filled with PEG electrolyte through an *in situ* thermal curing method (Fig. 13a). This approach not only accelerates ion transport but also ensures both the electrochemical stability and the flexibility of the system. Additionally, it was observed that at higher current densities up to 0.3 mA cm^{-2}, PEG and PVDF polymer electrolytes gradually become less stable while demonstrating the long cycle stability of PVDF@PEG electrolytes. The construction of this three-dimensional structure allowed us to achieve an ionic conductivity value of 1.06×10^{-3} S cm^{-1} at 100 °C (Fig. 13b), indicating its potential for practical applications.[174]

In another study by Yu *et al.*, they examined the higher diffusion coefficients of species such as Li$^+$, TFSI$^-$ and PVDF in polyol-based polymer electrolytes compared to those of their PVDF-based counterparts (Fig. 13c). Mean square displacement (MSD) analysis was used to determine their respective diffusion coefficients (Fig. 13d). In particular, the diffusion coefficient of Li$^+$ increased to 7.04×10^{-13} m^2 s^{-1} at room temperature, surpassing that observed in PVDF-based electrolytic systems, thus ensuring excellent compatibility between organic–inorganic combinations for positive electrodes.[175]

By coupling the ceramic medium with the PVDF-based electrolyte, more mobile Li$^+$ can be generated synchronously to establish an effective directional surface charge density; this addresses the challenge of low ionic conductivity. Shi *et al.* created a composite solid-state electrolyte (PVBL) by incorporating BaTiO$_3$–Li$_{0.33}$La$_{0.56}$TiO$_{3-x}$ nanowires into a poly(vinylidene difluoride) matrix, forming a side-by-side heterojunction structure (Fig. 13e). The presence of polarized dielectric BaTiO$_3$ promotes the dissociation of Li salt, facilitating the movement of Li$^+$ ions across the interface to facilitate efficient transport through coupled Li$_{0.33}$La$_{0.56}$TiO$_{3-x}$ regions. Furthermore, this combination suppresses the formation of the space charge layer with poly(vinylidene difluoride), resulting in an impressive ionic conductivity (8.2×10^{-4} S cm^{-1}) and the lithium transference number (0.57) for PVBL at 25 °C. In particular, when used as an interlayer between Li metal and PVL, PVBL reduces the overpotential due to the partial reduction of LLTO (from Ti^{4+} to Ti^{3+}) in PVL by Li metal, creating a mixed conductor interface that minimizes interfacial resistance.[176,177] COMSOL multiphysics simulations demonstrate that, compared to PVDF and PVL (Fig. 13f), PVBL achieves a more uniform potential distribution and negligible concentration polarization of Li$^+$ ions, while also homogenizing the interfacial electric field with electrodes. Solid state LiNi$_{0.8}$Co$_{0.1}$Mn$_{0.1}$O$_2$/PVBL/Li batteries cycle stably 1500 times at a current density of 180 mA h g^{-1}.[178]

Furthermore, Kang *et al.* reported another strategy involving salt polarization to fabricate highly ion-conductive SPEs using a high-dielectric polymer capable of strong interaction with lithium salts. Such a polymer with large dipole moments can guide lithium cations (Li$^+$) to align along the chain, forming a continuous pathway for Li$^+$ hopping within SSEs.[179] Similarly, Kang *et al.* enriched the dense thin layer on the anode side by incorporating highly dielectric asymmetrical poly(vinylidene fluoride)(PVDF)-PbZr$_x$Ti$_{1-x}$O$_3$ (PZT) nanoparticles with strong electronegativity at the dipole end. As shown in (Fig. 13g), this phenomenon attracts lithium ions (Li$^+$) at the PVDF–PZT interface and facilitates their transport through the dipole channel, promoting the dissociation of lithium salts into free Li$^+$ Furthermore, it somewhat increases the proportion of the amorphous zone as shown in (Fig. 13h).[180]

6.1   PVDF-HFP-based solid polymer electrolytes

A PVDF-HFP produced by the copolymerization of PVDF, which takes advantage of the increase in the proportion of the amorphous region of the copolymer to give it excellent electrochemical stability (Fig. 14f). Zhai *et al.* conducted a study on the challenges in polymer electrolytes by designing fluorinated graphene-reinforced PVDF-HFP-LiTFSI (FPH-Li) polymer electrolytes in a 2D structure. The incorporation of uniformly dispersed fluorinated graphene resulted in improved mechanical properties without significantly increasing the thickness of the polymer electrolyte (Fig. 14a). This was achieved through a unique grain refinement effect induced by fluorinated graphene, which enhanced the transport of interfacial lithium-ion (Li-ion) and homogenized Li ion flux. As a result, there was an enhancement in Li-ion conductivity and a promotion of uniform Li plating/stripping. Furthermore, extensive characterizations revealed that fluorinated graphene played a crucial role in the construction of a stable artificial interface, effectively preventing unwanted reactions between the lithium–metal anode and solvated molecules. Consequently, the use of thin FPH-Li polymer electrolytes with approximately 45 μm thickness facilitated long-term Li plating/stripping with minimal overpotential in symmetrical Li/Li cells and ensured stable cycling of full cells consisting of Li/LiNi$_{0.6}$Co$_{0.2}$Mn$_{0.2}$O$_2$ with a high average coulombic efficiency reaching 99.5% at 1.0 C.[181]

In PVDF-HFP-based electrolytes, there is interfacial instability caused by REDOX reactions between the electrolyte and the electrode, especially at high charge voltage or high temperature, which also leads to a large interfacial impedance generated by limited solid–solid rigid contact. Liu *et al.* developed a solid electrolyte called polymer-in-salt (PISSE) using PVDF-HFP. They used an integrated TiO$_2$/Li SSEs 3D fully permeable solid electrolyte model to construct it. PISSE exhibited faster Li$^+$ transport compared to conventional polymer electrolytes due to the formation of unique ion channels through aggregated ionic clusters, as shown in (Fig. 14b). Among a group of polymer electrolytes, this PISSE demonstrated the most favorable overall performance.[182]
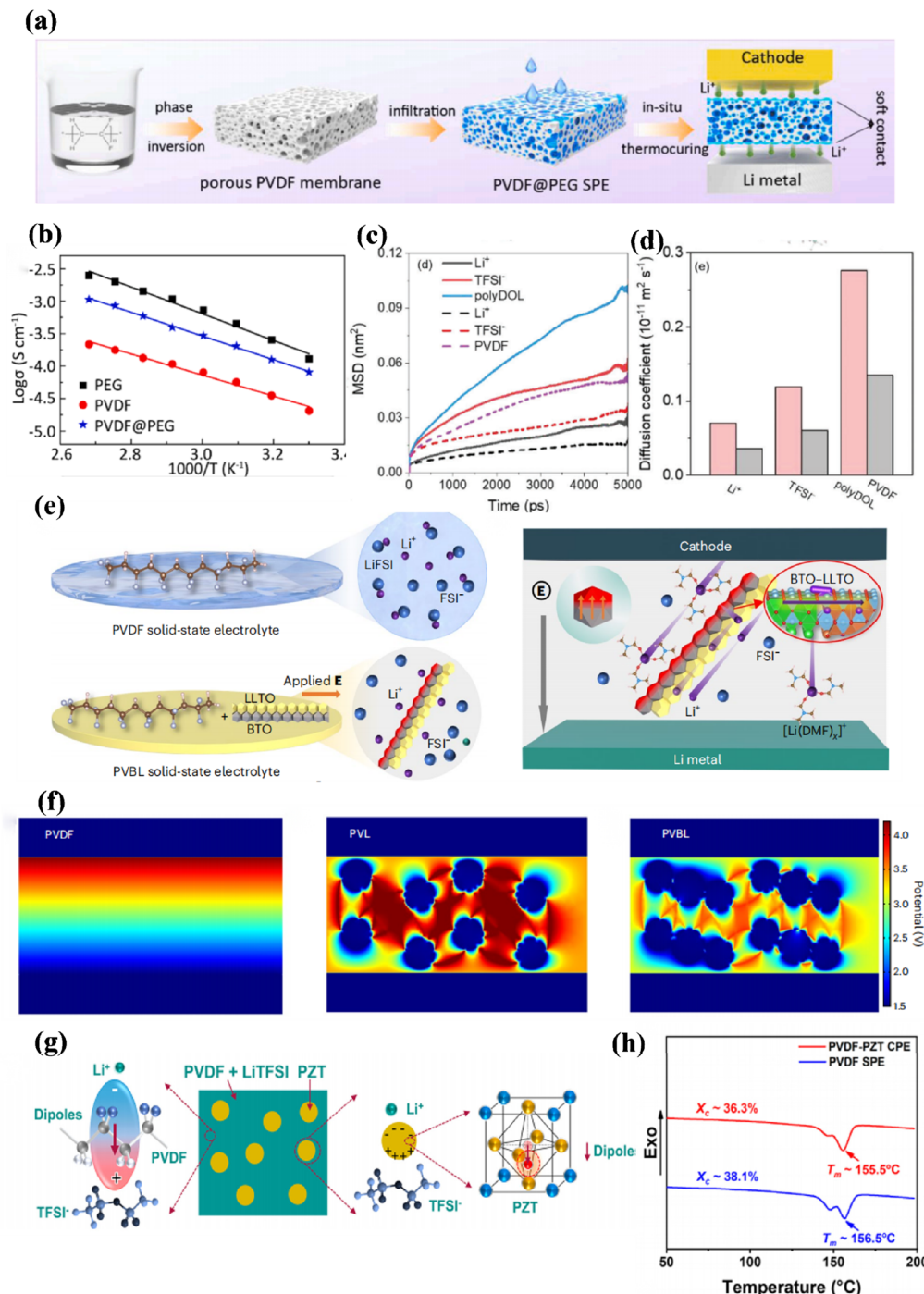
Fig. 13 (a) Preparation schematic of PVDF@PEG electrolyte, (b) Arrhenius plots of PEG, PVDF, and PVDF@PEG electrolytes at different temperatures ref. 174. Copyright 2022, Elsevier. (c) MSD *versus* time for the PVDF-based polymer electrolyte (dotted line) and polyDOL-based polymer electrolyte, (d) corresponding diffusion coefficients of the PVDF-based polymer electrolyte (grey) and the poly DOL-based polymer electrolyte (pink) ref. 175. Copyright 2022, Wiley-VCH. (e) Illustration of the Li salt dissociation and Li$^+$ transport by the coupled BTO-LLTO in the PVBL electrolyte, (f) COMSOL Multiphysics simulations of the potential distribution in PVDF ref. 178. Copyright 2022, Springer Nature. (g) Schematic diagram of the dipoles in PVDF and PZT in dissociating LiTFSI, (h) DSC spectra of the PVDF-PZT CPE and PVDF SPE ref. 180. Copyright 2022, Elsevier.

The formation of a homogenized electrolyte. Zhang *et al.* designed impressive composite SSEs that incorporate a PVDF-HFP matrix for good mechanical properties and Li salt solubility, a high content of lithium bis(fluorosulfonyl) imide (LiFSI) for an additional Li$^+$ hopping transmission path, and LLZTO filler for improved electrochemical stability, as shown in (Fig. 14c). As a result, this polymer-in-salt composite SSEs has an outstanding ionic conductivity of 1.67×10^{-3} S cm^{-1}
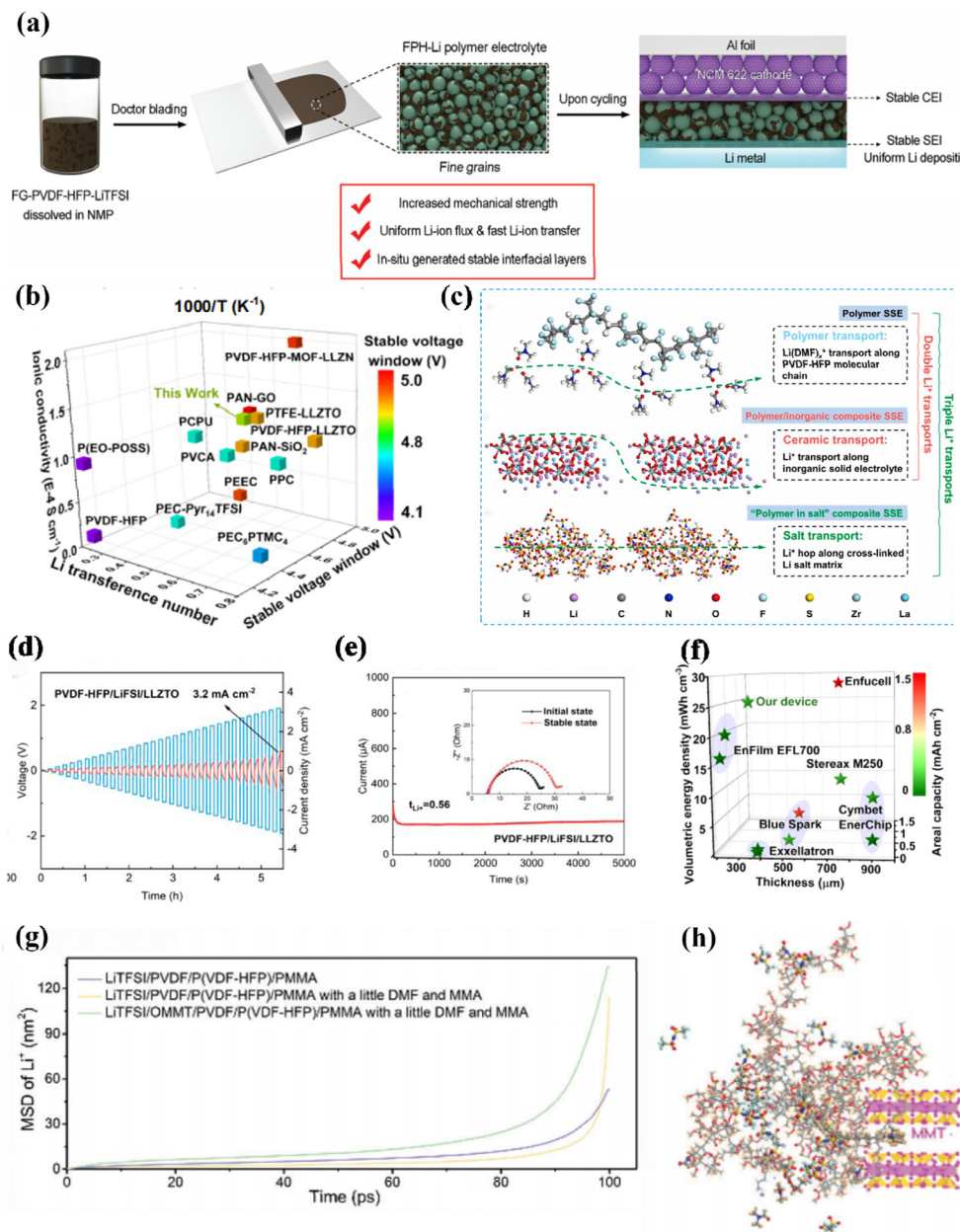
Fig. 14 (a) Schematic illustration of the influence of fluorinated graphene on the properties of polymer electrolytes ref. 181. Copyright 2022, Wiley-VCH. (b) Comparison of the reported conductivity of electrolyte ions ref. 182. Copyright 2021, Wiley-VCH. (c) Li$^+$ transport mechanism of bare polymer SSEs (single Li$^+$ transport path), polymer/inorganic composite SSEs (double Li$^+$ transport paths). "polymers in salt" composite SSE (triple Li$^+$ transport paths). (d) Critical current density test of PVDF-HFP/LiFSI/LLZTO electrolyte, (e) chronoamperometry curve of Li/FPH-Li/Li cell under 10 mV polarization ref. 183. Copyright 2023, Elsevier. (f) Compare the properties of various polymer matrices ref. 182. Copyright 2021, Wiley-VCH. (g) MD-simulated mean square displacement (MSD) of Li$^+$, (h) MD-simulated model curves of LOPPM PE ref. 184. Copyright 2023, Wiley-VCH.

and a superior critical current density (CCD) of 3.2 mA cm^{-2} at room temperature (25 °C), as illustrated in (Fig. 14d). Furthermore, the symmetric Li/Li battery displayed consistent polarization for up to 240 h at low current density and low capacity, as shown in (Fig. 14e).[183]

The researchers, Zhao *et al.* aimed to enhance the ionic conductivity at room temperature and optimize the charge/discharge performance for developing reusable polymer electrolytes (PEs). To achieve this, they utilized polyvinylidene fluor-

ide PVDF and a copolymer of PVDF-HFP, along with polymerized methyl methacrylate (MMA) monomers, as substrates in the preparation of the LiTFSI/OMMT/PVDF/PVDF-HFP/PMMA. The resulting LOPPM exhibited interconnected lithium-ion 3D network channels. The incorporation of organic-modified montmorillonite, which is rich in Lewis acid centers, facilitated the dissociation of lithium salt. (Fig. 14g) demonstrated how lithium ions could move within the composite system consisting of polymer-combined montmorillonite (OMMT).

Further analysis revealed an excess of negatively charged adsorbed cations on the surface of each lamella, as depicted in (Fig. 14h). Through compatibility with PVDF, OMMT was introduced into the PVDF-HFP block PVDF, leading to a material that was uniformly dispersed with unique multi-interfacial channels.[184]

7. Conclusion and prospect

In recent times, researchers have been increasingly focused on advancing the research of safe SSEs because of the inherent limitations of liquid electrolytes, such as their susceptibility to leakage, flammability, and toxicity. SSEs-based batteries are considered promising contenders for replacing current liquid batteries in the next generation. The key driver for the promotion of the applications of advanced ASSLBs lies in the development of high-performance materials specifically designed for solid-state electrolytes. In this regard, polymer electrolytes with exceptional processability can be seen as potential candidates for ASSLBs because of their remarkable chemical stability, optimal working range, and ionic conductivity.

This paper presents a comprehensive examination of the application of polymers with various chemical compositions in solid-state lithium batteries. The addition of inorganic fillers enhances the noncrystalline phase, although it poses challenges in terms of agglomeration and the achievement of uniform electrolytes. However, by incorporating a small quantity of liquid plasticizer modification, there is a significant improvement in ionic conductivity at the expense of the meticulous stability. Consequently, functional structures are devised through meticulous selection of polymers with distinct chemical architectures, such as one-dimensional nanofibers, two-dimensional nanolayers, and three-dimensional cross-linked skeletal frameworks.

Secondly, to increase the ionic conductivity of solid polymer electrolytes to that of liquid electrolytes, it is essential to establish extensive pathways for the transport of ion within the filler material. Regulation of ion transport is heavily dependent on factors such as the degree of crystallinity in the polymer matrix, considerations of free energy, and interactions among chain segments. Additionally, optimizing the interaction between the polymer electrolyte and the lithium salt can also significantly enhance cell performance. This objective can be accomplished through various approaches including incorporating various types of lithium salts and employing strategies involving polar salting.

Finally, the research progress of SPE in recent years is reviewed, including the types of polymer matrix, the corresponding modification methods, the interface detection, and the factors affecting the interface between solid polymer electrolyte and anode. We hope that this review provides an effective way to predict important breakthroughs in the development of new polymers, the addition of new functional polymers, or the use of additives in the near future.

Conflicts of interest

There are no conflicts to declare.

References

1 J. B. Goodenough and Y. Kim, *Chem. Mater.*, 2010, **22**, 587–603.
2 J. Janek and W. G. Zeier, *Nat. Energy*, 2016, **1**, 16141.
3 C.-M. Park and H.-J. Sohn, *Adv. Mater.*, 2007, **19**, 2465–2468.
4 T. Hasegawa, F. Bai, D. Mori, S. Taminato, Y. Takeda, O. Yamamoto, H. Izumi, H. Minami and N. Imanishi, *ChemElectroChem*, 2023, **10**, e202201043.
5 Y. Yao, X. Zhang, B. Li, C. Yan, P. Chen, J. Huang and Q. Zhang, *Materials*, 2020, **2**, 379–388.
6 Q. Kang, Z. Zhuang, Y. Liu, Z. Liu, Y. Li, B. Sun, F. Pei, H. Zhu, H. Li, P. Li, Y. Lin, K. Shi, Y. Zhu, J. Chen, C. Shi, Y. Zhao, P. Jiang, Y. Xia, D. Wang and X. Huang, *Adv. Mater.*, 2023, 2303460.
7 Z. Wang, L. Shen, S. Deng, P. Cui and X. Yao, *Adv. Mater.*, 2021, **33**, 2100353.
8 J. Hu, P. He, B. Zhang, B. Wang and L.-Z. Fan, *Energy Storage Mater.*, 2020, **26**, 283–289.
9 Q. Guo, F. Xu, L. Shen, Z. Wang, J. Wang, H. He and X. Yao, *J. Power Sources*, 2021, **498**, 229934.
10 Z. Gao, H. Sun, L. Fu, F. Ye, Y. Zhang, W. Luo and Y. Huang, Promises, *Adv. Mater.*, 2018, **30**, 1705702.
11 Q. Guo, F. Xu, L. Shen, S. Deng, Z. Wang, M. Li and X. Yao, *Energy Mater. Adv.*, 2022, **2022**, 9753506.
12 S. Tang, W. Guo and Y. Fu, *Adv. Energy Mater.*, 2021, **11**, 2000802.
13 T. K. Schwietert, V. A. Arszelewska, C. Wang, C. Yu, A. Vasileiadis, N. J. J. De Klerk, J. Hageman, T. Hupfer, I. Kerkamm, Y. Xu, E. Van Der Maas, E. M. Kelder, S. Ganapathy and M. Wagemaker, *Nat. Mater.*, 2020, **19**, 428–435.
14 J. Mindemark, M. J. Lacey, T. Bowden and D. Brandell, *Prog. Polym. Sci.*, 2018, **81**, 114–143.
15 J. Wu, L. Shen, Z. Zhang, G. Liu, Z. Wang, D. Zhou, H. Wan, X. Xu and X. Yao, *Electrochem. Energy Rev.*, 2021, **4**, 101–135.
16 P. Fan, H. Liu, V. Marosz, N. T. Samuels, S. L. Suib, L. Sun and L. Liao, *Adv. Funct. Mater.*, 2021, **31**, 2101380.
17 N. Piao, S. Liu, B. Zhang, X. Ji, X. Fan, L. Wang, P.-F. Wang, T. Jin, S.-C. Liou, H. Yang, J. Jiang, K. Xu, M. A. Schroeder, X. He and C. Wang, *ACS Energy Lett.*, 2021, **6**, 1839–1848.

18 F. Xu, S. Deng, Q. Guo, D. Zhou and X. Yao, *Small Methods*, 2021, **5**, 2100262.

19 N. Lu, X. Jing, Y. Xu, W. Lu, K. Liu and Z. Zhang, *ACTA PHYS. SIN.-CH ED*, 2023, 2207045.

20 J. Wu, S. Liu, F. Han, X. Yao and C. Wang, *Adv. Mater.*, 2021, **33**, 2000751.

21 J. Chen, J. Wu, X. Wang, A. Zhou and Z. Yang, *Energy Storage Mater.*, 2021, **35**, 70–87.

22 N. Lu, X. Jing, J. Zhang, P. Zhang, Q. Qiao and Z. Zhang, *Chem. Eng. J.*, 2022, **431**, 134001.

23 Y. Huang, K. Dai, J. Zhang and G. Dawson, *Chin. J. Catal.*, 2022, **43**, 2539–2547.

24 L. Ye and X. Li, *Nature*, 2021, **593**, 218–222.

25 M. Jiang, G. Liu, Q. Zhang, D. Zhou and X. Yao, *ACS Appl. Mater. Interfaces*, 2021, **13**, 18666–18672.

26 W. Li, Y. Li, X. Liu, Z. Gu, H. Liang, X. Zhao, J. Guo and X. Wu, *Adv. Funct. Mater.*, 2022, **32**, 2201038.

27 N. Zhang, J. He, W. Han and Y. Wang, *J. Mater. Sci.*, 2019, **54**, 9603–9612.

28 P. Dhatarwal and R. J. Sengwa, *Compos. Commun.*, 2020, **17**, 182–191.

29 W. Liu, S. W. Lee, D. Lin, F. Shi, S. Wang, A. D. Sendek and Y. Cui, *Nat. Energy*, 2017, **2**, 17035.

30 Q. Zhou, Q. Li, S. Liu, X. Yin, B. Huang and M. Sheng, *J. Power Sources*, 2021, **482**, 228929.

31 V. Augustyn, J. Come, M. A. Lowe, J. W. Kim, P.-L. Taberna, S. H. Tolbert, H. D. Abruña, P. Simon and B. Dunn, *Nat. Mater.*, 2013, **12**, 518–522.

32 Y. Lu, X. Huang, Z. Song, K. Rui, Q. Wang, S. Gu, J. Yang, T. Xiu, M. E. Badding and Z. Wen, *Energy Storage Mater.*, 2018, **15**, 282–290.

33 X. Jiang, J. Huang, Z. Bi, W. Ni, G. Gurzadyan, Y. Zhu and Z. Zhang, *Adv. Mater.*, 2022, **34**, 2109330.

34 H. Song, S. Xue, S. Chen, Z. Wang, Y. Song, J. Li, Z. Song, L. Yang and F. Pan, *Chin. J. Struct. Chem.*, 2022, **41**, 2205048–2205054.

35 K. Nie, X. Wang, J. Qiu, Y. Wang, Q. Yang, J. Xu, X. Yu, H. Li, X. Huang and L. Chen, *ACS Energy Lett.*, 2020, **5**, 826–832.

36 J. Bae, Y. Li, J. Zhang, X. Zhou, F. Zhao, Y. Shi, J. B. Goodenough and G. Yu, *Angew. Chem., Int. Ed.*, 2018, **57**, 2096–2100.

37 X. Xu, L. Wang, H. Fei and L. Ci, *J. Mater. Sci.: Mater. Electron.*, 2019, **30**, 19119–19125.

38 Z. Bi, S. Mu, N. Zhao, W. Sun, W. Huang and X. Guo, *Energy Storage Mater.*, 2021, **35**, 512–519.

39 S. Yi, T. Xu, L. Li, M. Gao, K. Du, H. Zhao and Y. Bai, *Solid State Ionics*, 2020, **355**, 115419.

40 B. Ziebarth, M. Klinsmann, T. Eckl and C. Elsässer, *Phys. Rev. B: Condens. Matter Mater. Phys.*, 2014, **89**, 174301.

41 A. Muralidharan, M. I. Chaudhari, L. R. Pratt and S. B. Rempe, *Sci. Rep.*, 2018, **8**, 10736.

42 A. Muralidharan, M. Chaudhari, S. Rempe and L. R. Pratt, *ECS Trans.*, 2017, **77**, 1155–1162.

43 B. Vorselaars, A. V. Lyulin, K. Karatasos and M. A. J. Michels, *Phys. Rev. E: Stat., Nonlinear, Soft Matter Phys.*, 2007, **75**, 011504.

44 X. Meng, Y. Liu, Y. Ma, Y. Boyjoo, J. Liu, J. Qiu and Z. Wang, *Adv. Mater.*, 2023, **35**, 2212039.

45 B. Zhao, R. Ran, M. Liu and Z. Shao, *Mater. Sci. Eng., R*, 2015, **98**, 1–71.

46 J. Jung, J. Ku, Y. S. Park, C.-H. Ahn, J.-H. Lee, S. S. Hwang and A. S. Lee, *Polym. Rev.*, 2022, **62**, 789–825.

47 W. Li, Y. Li, X. Liu, Z. Gu, H. Liang, X. Zhao, J. Guo and X. Wu, *Adv. Funct. Mater.*, 2022, **32**, 2201038.

48 M. Basappa, H. Ganesha, S. Veeresh, Y. S. Nagaraju, M. Vandana, H. Vijeth and H. Devendrappa, *Chem. Phys. Lett.*, 2022, **799**, 139609.

49 A. Muralidharan, M. I. Chaudhari, S. B. Rempe and L. R. Pratt, *ECS Trans.*, 2017, **77**, 1155–1162.

50 B. Vorselaars, A. V. Lyulin, K. Karatasos and M. A. Michels, *Phys. Rev. E: Stat., Nonlinear, Soft Matter Phys.*, 2007, **75**, 011504.

51 A. Muralidharan, M. I. Chaudhari, L. R. Pratt and S. B. Rempe, *Sci. Rep.*, 2018, **8**, 10736.

52 C. Monroe and J. Newman, *J. Electrochem. Soc.*, 2003, **150**, 10–A1377.

53 Y. Lu, X. Huang, Z. Song, K. Rui, Q. Wang, S. Gu, J. Yang, T. Xiu and M. E. Badding, *Energy Storage Mater.*, 2018, **15**, 282–290.

54 P. Barai, K. Higa, A. T. Ngo, L. A. Curtiss and V. Srinivasan, *J. Electrochem. Soc.*, 2019, **166**, A1752–A1762.

55 S. Yu and D. J. Siegel, *ACS Appl. Mater. Interfaces*, 2018, **10**, 38151–38158.

56 X. Huang, Y. Lu, Z. Song, T. Xiu, M. E. Badding and Z. Wen, *J. Energy Chem.*, 2019, **39**, 8–16.

57 Y. Lu, X. Huang, Y. Ruan, Q. Wang, R. Kun, J. Yang and Z. Wen, *J. Mater. Chem. A*, 2018, **6**, 18853–18858.

58 X. Huang, Y. Lu, Z. Song, K. Rui, Q. Wang, T. Xiu, M. E. Badding and Z. Wen, *Energy Storage Mater.*, 2019, **22**, 207–217.

59 W. Ping, C. Wang, Z. Lin, E. Hitz, C. Yang, H. Wang and L. Hu, *Adv. Energy Mater.*, 2020, **10**, 2000702.

60 S. Lee, K. Lee, S. Kim, K. Yoon, S. Han, M. H. Lee, Y. Ko, J. H. Noh, W. Kim and K. Kang, *Sci. Adv.*, 2022, **8**, eabq0153.

61 H. Xu, J. Zhang, H. Zhang, J. Long, L. Xu and L. Mai, *Adv. Energy Mater.*, 2023, **13**, 2204411.

62 L. Hu, X. Gao, Z. Li, Y. Liu, H. Wang, J. Liu and R. Hu, *ACS Appl. Mater. Interfaces*, 2023, **15**, 38485–38495.

63 M. Ge, X. Zhou, Y. Qin, Y. Liu, J. Zhou, X. Wang and B. Guo, *Chin. Chem. Lett.*, 2022, **33**, 3894–3898.

64 X. Zhang, Y. Sun, C. Ma, N. Guo, H. Fan, J. Liu and H. Xie, *J. Power Sources*, 2022, **542**, 231797.

65 Z. Bi, S. Mu, N. Zhao, W. Sun, W. Huang and X. Guo, *Energy Storage Mater.*, 2021, **35**, 512–519.

66 R. Kumar, S. Sharma, D. Pathak, N. Dhiman and N. Arora, *Solid State Ionics*, 2017, **305**, 57–62.

67 J. Chen and S. Han, *Chem. Eng. J.*, 2023, **470**, 144150.

68 J. Wei, X. Zheng, W. Lin, Y. Si, K. Ji, C. Wang and M. Chen, *J. Alloys Compd.*, 2022, **909**, 164825.

69 Y. G. Choi, J. C. Shin, A. Park, Y. M. Jeon, J. I. Kim, S. Kim, S. Kim, W. B. Lee, M. Lee and J. H. Park, *Adv. Energy Mater.*, 2021, **11**, 2102660.

70 S. Li, K. Jiang, J. Wang, C. Zuo, Y. H. Jo, D. He, X. Xie and Z. Xue, *Macromolecules*, 2019, **52**, 7234–7243.

71 S. Y. An, X. Wu, Y. Zhao, T. Liu, R. Yin, J. H. Ahn, L. M. Walker, J. F. Whitacre and K. Matyjaszewski, *Adv. Sci.*, 2023, e2302932.

72 F. Fu, Y. Zheng, N. Jiang, Y. Liu, C. Sun, A. Zhang, H. Teng, L. Sun and H. Xie, *Chem. Eng. J.*, 2022, **450**, 137776.

73 Y. Xu, J. Li and W. Li, *Colloids Surf., A*, 2022, **632**, 127773.

74 Q. Ye, H. Liang, S. Wang, C. Cui, C. Zeng, T. Zhai and H. Li, *J. Energy Chem.*, 2022, **70**, 356–362.

75 S. J. Wen, T. J. Richardson, D. I. Ghantous, K. A. Striebel, P. N. Ross and E. J. Cairns, *J. Electroanal. Chem.*, 1996, **408**, 113–118.

76 Y. Mallaiah, V. R. Jeedi, R. Swarnalatha, A. Raju and S. Narender Reddy, *J. Phys. Chem. Solids*, 2021, **155**, 110096.

77 J. Qiu, X. Liu, R. Chen, Q. Li, Y. Wang, P. Chen, L. Gan, S. J. Lee, D. Nordlund, Y. Liu, X. Yu, X. Bai, H. Li and L. Chen, *Adv. Funct. Mater.*, 2020, **30**, 1909392.

78 S. Wang, Y. Chen, Q. Fang, J. Huang, X. Wang, S. Chen and S. Zhang, *Energy Storage Mater.*, 2023, **54**, 596–604.

79 D. E. Fenton, J. M. Parker and P. V. Wright, *Polymer*, 1973, **14**, 589.

80 D. Cai, D. Wang, Y. Chen, S. Zhang, X. Wang, X. Xia and J. Tu, *Chem. Eng. J.*, 2020, **394**, 124993.

81 V. Selvanathan, M. N. A. Halim, A. D. Azzahari, M. Rizwan, N. Shahabudin and R. Yahya, *Ionics*, 2018, **24**, 1955–1964.

82 F. Li, B. Su, L. Shi, J. Mu, F. Xu, J. Wang, H. Yang and Z. Guo, *Ceram. Int.*, 2023, **49**, 26604–26615.

83 X. Cai, J. Ding, Z. Chi, W. Wang, D. Wang and G. Wang, *ACS Nano*, 2021, **15**, 20489–20503.

84 H. Zhuang, W. Ma, J. Xie, X. Liu, B. Li, Y. Jiang, S. Huang, Z. Chen and B. Zhao, *J. Alloys Compd.*, 2021, **860**, 157915.

85 J. Yin, X. Xu, S. Jiang, Y. Lei and Y. Gao, *J. Power Sources*, 2022, **550**, 232139.

86 A. Kondori, M. Esmaeilirad, A. M. Harzandi, R. Amine, M. T. Saray, L. Yu and M. Asadi, *Science*, 2023, **379**, 499–505.

87 M. Zhang, K. Zhou, D. Ma, H. Wang, X. Tang, M. Bai, F. Liu, Z. Wang and Y. Ma, *Mater. Today*, 2022, **56**, 53–65.

88 P. Chen, J. Shen, T. Wang, M. Dai, C. Si, J. Xie, M. Li, X. Cong and X. Sun, *J. Power Sources*, 2018, **400**, 325–332.

89 J. Shen, Z. Lei and C. Wang, *Chem. Eng. J.*, 2022, **447**, 137503.

90 L. Gao, S. Luo, J. Li, B. Cheng, W. Kang and N. Deng, *Energy Storage Mater.*, 2021, **43**, 266–274.

91 L. Gao, J. Li, J. Ju, B. Cheng, W. Kang and N. Deng, *J. Energy Chem.*, 2021, **54**, 644–654.

92 Q. Yang, G. Li, D. Shi, L. Gao, N. Deng, W. Kang and B. Cheng, *Small*, 2023, 2301521.

93 Y. Zhao, J. Yan, W. Cai, Y. Lai, J. Song, J. Yu and B. Ding, *Energy Storage Mater.*, 2019, **23**, 306–313.

94 J. Shin, W.-H. Ryu, K.-S. Park and I.-D. Kim, *ACS Nano*, 2013, **7**, 7330–7341.

95 Y. Li, Z. Fu, S. Lu, X. Sun, X. Zhang and L. Weng, *Chem. Eng. J.*, 2022, **440**, 135816.

96 H. Y. Sun, Y. Takeda, N. Imanishi, O. Yamamoto and H.-J. Sohn, *J. Electrochem. Soc.*, 2000, **147**, 2462.

97 T. Itoh, *Solid State Ionics*, 2003, **156**, 393–399.

98 T. Itoh, Y. Miyamura, Y. Ichikawa, T. Uno, M. Kubo and O. Yamamoto, *J. Power Sources*, 2003, **119–121**, 403–408.

99 J. Kang, Z. Yan, L. Gao, Y. Zhang, W. Liu, Q. Yang, Y. Zhao, N. Deng, B. Cheng and W. Kang, *Energy Storage Mater.*, 2022, **53**, 192–203.

100 H. Chen, D. Adekoya, L. Hencz, J. Ma, S. Chen, C. Yan, H. Zhao, G. Cui and S. Zhang, *Adv. Energy Mater.*, 2020, **10**, 2000049.

101 L. Zhang, N. Deng, J. Kang, X. Wang, H. Gao, Y. Liu, H. Wang, G. Wang, B. Cheng and W. Kang, *J. Energy Chem.*, 2023, **77**, 326–337.

102 B. Xu, X. Li, C. Yang, Y. Li, N. S. Grundish, P.-H. Chien, K. Dong, I. Manke, R. Fang, N. Wu, H. Xu, A. Dolocan and J. B. Goodenough, *J. Am. Chem. Soc.*, 2021, **143**, 6542–6550.

103 X. Wang, Y. Song, X. Jiang, Q. Liu, J. Dong, J. Wang, X. Zhou, B. Li, G. Yin, Z. Jiang and J. Wang, *Adv. Funct. Mater.*, 2022, **32**, 2113068.

104 L. Xu, X. Xiao, H. Tu, F. Zhu, J. Wang, H. Liu, W. Huang, W. Deng, H. Hou, T. Liu, X. Ji, K. Amine and G. Zou, *Adv. Mater.*, 2023, 2303193.

105 Q. Pan, Y. Zheng, S. Kota, W. Huang, S. Wang, H. Qi, S. Kim, Y. Tu, M. W. Barsoum and C. Y. Li, *Nanoscale Adv.*, 2019, **1**, 395–402.

106 Y. Shi, B. Li, Q. Zhu, K. Shen, W. Tang, Q. Xiang, W. Chen, C. Liu, J. Luo and S. Yang, *Adv. Energy Mater.*, 2020, **10**, 1903534.

107 Y. Zhang, Y. Wu, Y. Liu and J. Feng, *Chem. Eng. J.*, 2022, **428**, 131040.

108 Z. Li, W.-X. Sha and X. Guo, *ACS Appl. Mater. Interfaces*, 2019, **11**, 26920–26927.

109 H. Zhai, P. Xu, M. Ning, Q. Cheng, J. Mandal and Y. Yang, *Nano Lett.*, 2017, **17**, 3182–3187.

110 J. Bae, Y. Li, F. Zhao, X. Zhou, Y. Ding and G. Yu, *Energy Storage Mater.*, 2018, **15**, 46–52.

111 X. Zuo, K. Chang, J. Zhao, Z. Xie, H. Tang, B. Li and Z. Chang, *J. Mater. Chem. A*, 2016, **4**, 51–58.

112 Y. Yan, J. Ju, S. Dong, Y. Wang, L. Huang, L. Cui, F. Jiang, Q. Wang, Y. Zhang and G. Cui, *Adv. Sci.*, 2021, **8**, 2003887.

113 X. Wang, H. Zhai, B. Qie, Q. Cheng, A. Li, J. Borovilas, B. Xu, C. Shi, T. Jin, X. Liao, Y. Li, X. He, S. Du, Y. Fu, M. Dontigny, K. Zaghib and Y. Yang, *Nano Energy*, 2019, **60**, 205–212.

114 S. Cheng, D. M. Smith and C. Y. Li, *Macromolecules*, 2015, **48**, 4503–4510.

115 X. Tian and B. Xu, *Small Methods*, 2021, **5**, 2100877.

116 G. Wang, H. Liu, Y. Liang, C. Wang and L.-Z. Fan, *Energy Storage Mater.*, 2022, **45**, 1212–1219.

117 Y. Liu, L. Han, C. Liao, H. Yu, Y. Kan and Y. Hu, *Chem. Eng. J.*, 2023, **468**, 143222.

118 D. Lin, P. Y. Yuen, Y. Liu, W. Liu, N. Liu, R. H. Dauskardt and Y. Cui, *Adv. Mater.*, 2018, **30**, 1802661.

119 H. Yang, X. Chen, N. Yao, N. Piao, Z. Wang, K. He, H.-M. Cheng and F. Li, *ACS Energy Lett.*, 2021, 1413–1421.

120 S.-J. Yang, N. Yao, X.-Q. Xu, F.-N. Jiang, X. Chen, H. Liu, H. Yuan, J.-Q. Huang and X.-B. Cheng, *J. Mater. Chem. A*, 2021, **9**, 19664–19668.

121 N. Piao, S. Liu, B. Zhang, X. Ji, X. Fan, L. Wang, P.-F. Wang, T. Jin, S.-C. Liou, H. Yang, J. Jiang, K. Xu, M. A. Schroeder, X. He and C. Wang, *ACS Energy Lett.*, 2021, **6**, 1839–1848.

122 D. Xiao, Q. Li, D. Luo, G. Li, H. Liu, L. Shui, S. Gourley, G. Zhou, X. Wang and Z. Chen, *Small*, 2020, **16**, 2004688.

123 J. Mindemark, E. Törmä, B. Sun and D. Brandell, *Polymer*, 2015, **63**, 91–98.

124 M. P. Rosenwinkel, R. Andersson, J. Mindemark and M. Schönhoff, *J. Phys. Chem. C*, 2020, **124**, 23588–23596.

125 J. Mindemark, B. Sun, E. Törmä and D. Brandell, *J. Power Sources*, 2015, **298**, 166–170.

126 B. Zhang, Y. Liu, J. Liu, L. Sun, L. Cong, F. Fu, A. Mauger, C. M. Julien, H. Xie and X. Pan, *J. Energy Chem.*, 2021, **52**, 318–325.

127 C. Sångeland, G. Hernández, D. Brandell, R. Younesi, M. Hahlin and J. Mindemark, *ACS Appl. Mater. Interfaces*, 2022, **14**, 28716–28728.

128 Y. Chen, Y. Zhang, J. Niu, H. Xu, Z. Dong, J. Xu and C. Lei, *ACS Appl. Energy Mater.*, 2023, **6**, 3113–3125.

129 F. P. Nkosi, M. Valvo, J. Mindemark, N. A. Dzulkurnain, G. Hernández, A. Mahun, S. Abbrent, J. Brus, L. Kobera and K. Edström, *ACS Appl. Energy Mater.*, 2021, **4**, 2531–2542.

130 S.-B. Hong, Y.-J. Lee, U.-H. Kim, C. Bak, Y. M. Lee, W. Cho, H. J. Hah, Y.-K. Sun and D.-W. Kim, *ACS Energy Lett.*, 2022, **7**, 1092–1100.

131 S. T. Oyakhire, H. Gong, Y. Cui, Z. Bao and S. F. Bent, *ACS Energy Lett.*, 2022, **7**, 2540–2546.

132 E. Markevich, G. Salitra and D. Aurbach, *ACS Energy Lett.*, 2017, **2**, 1337–1345.

133 W. Huang, H. Wang, D. T. Boyle, Y. Li and Y. Cui, *ACS Energy Lett.*, 2020, **5**, 1128–1135.

134 A. M. Elmér and P. Jannasch, *J. Polym. Sci., Part A: Polym. Chem.*, 2006, **44**, 2195–2205.

135 C. Wang, H. Liu, Y. Liang, D. Li, X. Zhao, J. Chen, W. Huang, L. Gao and L. Fan, *Adv. Funct. Mater.*, 2023, **33**, 2209828.

136 O. B. Chae and B. L. Lucht, *Adv. Energy Mater.*, 2023, **13**, 2203791.

137 K. Vignarooban, M. A. K. L. Dissanayake, I. Albinsson and B.-E. Mellander, *Solid State Ionics*, 2014, **266**, 25–28.

138 X. Wang, Y. Zhang, X. Zhang, T. Liu, Y.-H. Lin, L. Li, Y. Shen and C.-W. Nan, *ACS Appl. Mater. Interfaces*, 2018, **10**, 24791–24798.

139 K. He, S. H. Cheng, J. Hu, Y. Zhang, H. Yang, Y. Liu, W. Liao, D. Chen, C. Liao, X. Cheng, Z. Lu, J. He, J. Tang, R. K. Y. Li and C. Liu, *Angew. Chem., Int. Ed.*, 2021, **60**, 12116–12123.

140 X. Zuo, K. Chang, J. Zhao, Z. Xie, H. Tang, B. Li and Z. Chang, *J. Mater. Chem. A*, 2016, **4**, 51–58.

141 Y. Zheng, X. Li and C. Y. Li, *Energy Storage Mater.*, 2020, **29**, 42–51.

142 J. Zhang, J. Yang, T. Dong, M. Zhang, J. Chai, S. Dong, T. Wu, X. Zhou and G. Cui, *Small*, 2018, **14**, 1800821.

143 Z. Li, H. Zhang, X. Sun and Y. Yang, *ACS Energy Lett.*, 2020, **5**, 3244–3253.

144 L. Zhu, J. Li, Y. Jia, P. Zhu, M. Jing, S. Yao, X. Shen, S. Li and F. Tu, *Int. J. Energy Res.*, 2020, **44**, 10168–10178.

145 H. Chen, M. Jing, C. Han, H. Yang, S. Hua, F. Chen, L. Chen, Z. Zhou, B. Ju, F. Tu, X. Shen and S. Qin, *Int. J. Energy Res.*, 2019, **43**, 5912–5921.

146 M. Jia, N. Zhao, Z. Bi, Z. Fu, F. Xu, C. Shi and X. Guo, *ACS Appl. Mater. Interfaces*, 2020, **12**, 46162–46169.

147 B.-J. Sung, P. N. Didwal, R. Verma, A.-G. Nguyen, D. R. Chang and C.-J. Park, *Electrochim. Acta*, 2021, **392**, 139007.

148 S. Luo, E. Zhao, Y. Gu, J. Huang, Z. Zhang, L. Yang and S. Hirano, *Chem. Eng. J.*, 2021, **421**, 127771.

149 S. Wang, Q. Sun, Q. Zhang, C. Li, C. Xu, Y. Ma, X. Shi, H. Zhang, D. Song and L. Zhang, *Adv. Energy Mater.*, 2023, **13**, 2204036.

150 Q. Lu, J. Fang, J. Yang, G. Yan, S. Liu and J. Wang, *J. Membr. Sci.*, 2013, **425–426**, 105–112.

151 S. Xu, Z. Sun, C. Sun, F. Li, K. Chen, Z. Zhang, G. Hou, H. Cheng and F. Li, *Adv. Funct. Mater.*, 2020, **30**, 2007172.

152 Q. Zhou, J. Ma, S. Dong, X. Li and G. Cui, *Adv. Mater.*, 2019, **31**, 1902029.

153 Q. Zhang, K. Liu, F. Ding, W. Li, X. Liu and J. Zhang, *ACS Appl. Mater. Interfaces*, 2017, **9**, 29820–29828.

154 F. Fu, Y. Liu, C. Sun, L. Cong, Y. Liu, L. Sun and H. Xie, *Energy Environ. Mater.*, 2023, **6**, e12367.

155 M. Zuo, Z. Bi and X. Guo, *Chem. Eng. J.*, 2023, **463**, 142463.

156 D. Bao, Y. Tao, Y. Zhong, W. Zhao, M. Peng, H. Zhang and X. Sun, *Adv. Funct. Mater.*, 2023, **33**, 2213211.

157 M. J. Lee, J. Han, K. Lee, Y. J. Lee, B. G. Kim, K.-N. Jung, B. J. Kim and S. W. Lee, *Nature*, 2022, **601**, 217–222.

158 F. Urbain, V. Smirnov, J.-P. Becker, A. Lambertz, F. Yang, J. Ziegler, B. Kaiser, W. Jaegermann, U. Rau and F. Finger, *Energy Environ. Sci.*, 2016, **9**, 145–154.

159 L. N. Sim, F. C. Sentanin, A. Pawlicka, R. Yahya and A. K. Arof, *Electrochim. Acta*, 2017, **229**, 22–30.

160 X. Wang, X. Hao, Y. Xia, Y. Liang, X. Xia and J. Tu, *Science*, 2019, **582**, 37–47.

161 N. K. Jyothi, K. K. V. Ratnam, P. N. Murthy and K. V. Kumar, *Mater. Today: Proc.*, 2016, **3**, 21–30.

162 R. Rojaee, S. Cavallo, S. Mogurampelly, B. K. Wheatle, V. Yurkiv, R. Deivanayagam, T. Foroozan, M. G. Rasul, S. Sharifi-Asl, A. H. Phakatkar, M. Cheng, S. Son, Y. Pan, F. Mashayek, V. Ganesan and R. Shahbazian-Yassar, *Adv. Funct. Mater.*, 2020, **30**, 1910749.

163 S. Chai, Z. Chang, Y. Zhong, Q. He, Y. Wang, Y. Wan, M. Feng, Y. Hu, W. Li, W. Wei and A. Pan, *Adv. Funct. Mater.*, 2023, **33**, 2300425.

164 P. Raghavan, X. Zhao, C. Shin, D.-H. Baek, J.-W. Choi, J. Manuel, M.-Y. Heo, J.-H. Ahn and C. Nah, *J. Power Sources*, 2010, **195**, 6088–6094.

165 X. Wang, Y. Fang, X. Yan, S. Liu, X. Zhao and L. Zhang, *Polymer*, 2021, **230**, 124038.

166 D. Li, L. Chen, T. Wang and L.-Z. Fan, *ACS Appl. Mater. Interfaces*, 2018, **10**, 7069–7078.

167 X.-L. Zhang, F.-Y. Shen, X. Long, S. Zheng, Z. Ruan, Y.-P. Cai, X.-J. Hong and Q. Zheng, *Energy Storage Mater.*, 2022, **52**, 201–209.

168 S. Bandyopadhyay, A. Gupta, R. Srivastava and B. Nandan, *Chem. Eng. J.*, 2022, **440**, 135926.

169 Z. Li, S. Wang, J. Shi, Y. Liu, S. Zheng, H. Zou, Y. Chen, W. Kuang, K. Ding, L. Chen, Y. Lan, Y. Cai and Q. Zheng, *Energy Storage Mater.*, 2022, **47**, 262–270.

170 X. Zhang, Q. Su, G. Du, B. Xu, S. Wang, Z. Chen, L. Wang, W. Huang and H. Pang, *Angew. Chem., Int. Ed.*, 2023, e202304947.

171 J. Li, K. Zhu, Z. Yao, G. Qian, J. Zhang, K. Yan and J. Wang, *Ionics*, 2020, **26**, 1101–1108.

172 S. Yi, T. Xu, L. Li, M. Gao, K. Du, H. Zhao and Y. Bai, *Solid State Ionics*, 2020, **355**, 115419.

173 J. Xi, X. Qiu and L. Chen, *Solid State Ionics*, 2006, **177**, 709–713.

174 Z. Wang, Q. Guo, R. Jiang, S. Deng, J. Ma, P. Cui and X. Yao, *Chem. Eng. J.*, 2022, **435**, 135106.

175 J. Yu, G. Zhou, Y. Li, Y. Wang, D. Chen and F. Ciucci, *Small*, 2023, 2302691.

176 K. Yang, L. Chen, J. Ma, Y. He and F. Kang, *InfoMat*, 2021, **3**, 1195–1217.

177 W. Guo, S. Liu, X. Guan, X. Zhang, X. Liu and J. Luo, *Adv. Energy Mater.*, 2019, **9**, 1900193.

178 P. Shi, J. Ma, M. Liu, S. Guo, Y. Huang, S. Wang, L. Zhang, L. Chen, K. Yang, X. Liu, Y. Li, X. An, D. Zhang, X. Cheng, Q. Li, W. Lv, G. Zhong, Y.-B. He and F. Kang, *Nat. Nanotechnol.*, 2023, **18**, 602–610.

179 B.-H. Kang, S.-F. Li, J. Yang, Z.-M. Li and Y.-F. Huang, *ACS Nano*, 2023, **17**, 14114–14122.

180 Q. Kang, Y. Li, Z. Zhuang, D. Wang, C. Zhi, P. Jiang and X. Huang, *J. Energy Chem.*, 2022, **69**, 194–204.

181 P. Zhai, Z. Yang, Y. Wei, X. Guo and Y. Gong, *Adv. Energy Mater.*, 2022, **12**, 2200967.

182 W. Liu, C. Yi, L. Li, S. Liu, Q. Gui, D. Ba, Y. Li, D. Peng and J. Liu, *Angew. Chem., Int. Ed.*, 2021, **60**, 12931–12940.

183 J. Zhang, Y. Zeng, Q. Li, Z. Tang, D. Sun, D. Huang, L. Zhao, Y. Tang and H. Wang, *Energy Storage Mater.*, 2023, **54**, 440–449.

184 Y. Zhao, L. Li, Y. Shan, D. Zhou, X. Chen, W. Cui and H. Wang, *Small*, 2023, 2301572.